Moritz Paul Karl Frewein, Bsc

Global X-ray scattering data analysis of inverted hexagonal phases to measure intrinsic lipid curvatures

MASTERARBEIT

zur Erlangung des akademischen Grades

Master of Science

Masterstudium Technische Physik

eingereicht an der

Technischen Universität Graz

Betreuer

Assoz. Prof. Dipl.-Ing. Dr.techn.
Georg Pabst

Institut für Materialphysik

Graz, April 2018

EIDESSTATTLICHE ERKLÄRUNG

Ich erkläre an Eides statt, dass ich die vorliegende Arbeit selbstständig verfasst, andere als die angegebenen Quellen/Hilfsmittel nicht benutzt, und die den benutzten Quellen wörtlich und inhaltlich entnommenen Stellen als solche kenntlich gemacht habe. Das in TUGRAZonline hochgeladene Textdokument ist mit der vorliegenden Masterarbeit identisch.

Datum	Unterschrift

Acknowledgement

I wish to thank, first and foremost, my Professor Georg Pabst for giving me the opportunity to conduct this research, for the trust and support I received in the course of the work, for taking me to very interesting and enjoyable conferences, for (almost) always having the door of his office open and - last but not least - for the help with my future employment.

I would also like to share a large part of the credit of my work with the rest of the biophysics group. I want to thank Michael Pachler for the introduction to the laboratory and for countless conversations about theory and programming. It was an honor to work beside Barbara Eicher, whom I asked far too many questions in the beginning of my work, and i wish her all the best for her life within and apart from research. Thanks to Michal Belička for the phrase "Always question your model!", which will probably resonate in my head for many years.

Thanks to Primož Ziherl for his considerations about curvature addition and to Otto Glatter for trying his method for our system. I would also like to express my deepest gratitude to Michael Rumetshofer from the theory department for assisting me with the Monte Carlo algorithm.

I acknowledge the immense support that I have always received by my family, especially my parents who made my physics studies possible. I thank my grandmother for cooking for me every week, Wolfgang for printing this work and Minami for bearing with me after exhausting working days.

Abstract

Intrinsic curvature C_0 is a property of lipids, which describes the bending radius of unstressed monolayers. It is an important parameter in the calculation of interfacial energies, which affect lipid/protein interactions or interleaflet coupling in asymmetric lipid membranes. Intrinsic lipid curvatures are frequently determined using small-angle X-ray scattering (SAXS) experiments on inverted hexagonal phases (H_{II}) of dioleoyl phosphatidylethanolamine (DOPE) templates with various amounts of non-H_{II} forming host lipids. A basic assumption of this approach is a linear addivity of the individual C_0 values. Due to diverse lipid headgroup interactions this may not always be justified, however. Moreover, temperature effects or repulsive interactions between lipids rapidly decrease the scattering signal of H_{II} phases adding another limitation to this approach. In order to seek for a method to circumvent these issues we explored a full q-range SAXS data analysis method that also takes into account experimentally observed diffuse scattering contributions. Further, we included a non-linearity term for lipid mixtures based on the effective lipid headgroup size. This allows to retrieve intrinsic curvatures from weakly ordered H_{II} phases and minimizes the amount of samples required. This thesis gives an overview over the experiment, model and possible data evaluation techniques.

Contents

List of Figures

List of Tables

1 Introduction

This thesis is dedicated to the investigation of lipid molecules by X-ray diffraction experiments. Measuring the shape of molecules within biological aggregates holds a lot of difficulties, due to the complexity of particle interactions and the high spatial uncertainties within the liquid crystalline state. Former methods to measure the spontaneous curvature of lipids required multiple measurements with different lipid concentrations and the extrapolation of the desired values.
[1, 2] In this work we are testing a model-based approach to measure spontaneous curvatures of one or two lipids with a single experiment.

1.1 Lipids

Lipids are one of the most important structure giving groups of molecules in biology. They are essential for the formation of cell membranes. The crucial physical feature in their structure is their amphiphilic nature, given by a polar headgroup and one or more unpolar tails. As an example, a *glycerophospholipid* is shown in figure 1.1.

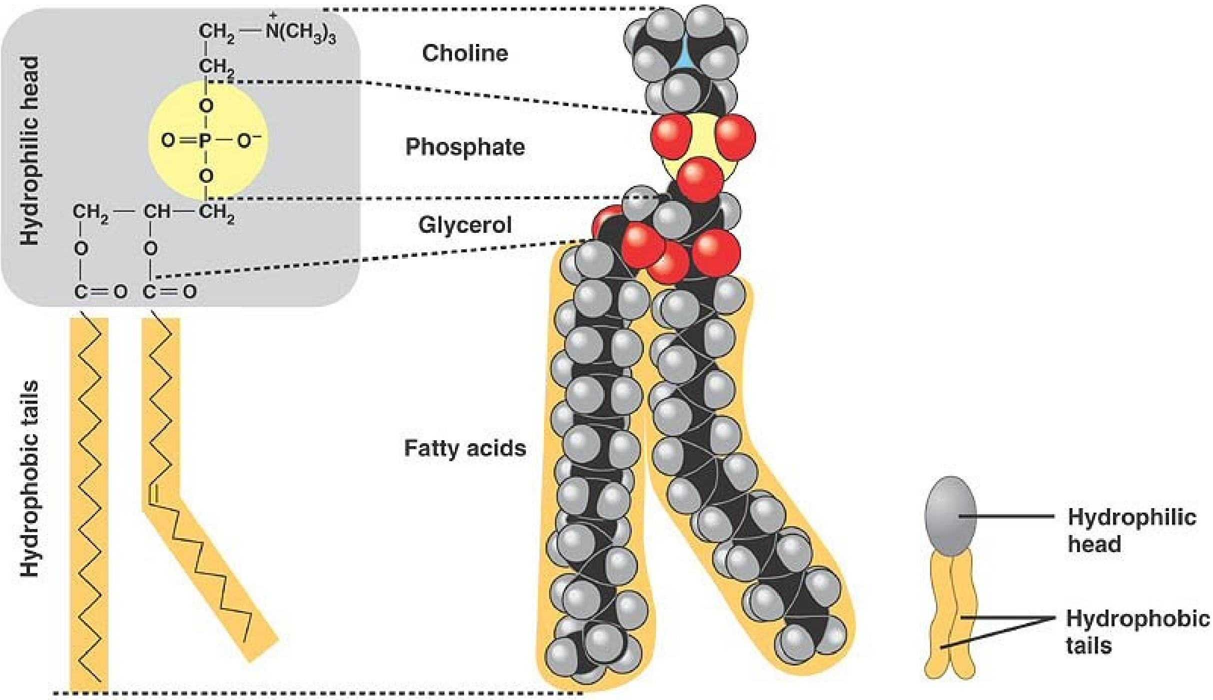

Figure 1.1: Chemical structure, Van der Waals-model and a simplified representation of a glycerophospholipid[3].

Tail groups are always made of aliphatic compounds, like saturated or unsaturated hydrocarbon chains (fatty acids). Fatty acids are often labelled as XX:Y, where XX denotes the number of carbon atoms and Y the degree of unsaturation (= number of double bonds).
The lipids of our interest are *phospholipids*. They have their hydrocarbon chain(s) attached to a *glycerol* backbone in the case of *glycerolipids* or to the long chain amine *sphingosine* in *sphingolipids*. Attached to the backbone is a a negatively charged *phosphate* group (PO_4), which is

often linked to a positively charged front part, like *choline*.

Lipids are designed to form structures in aqueous solutions. Due to the amphiphilic character, they self-assemble into micelles, bilayers or more complex structures (figure 1.2, 1.4). The headgroups arrange next to each other along the oil-water interface, to shield the tails from contact with water.[4]

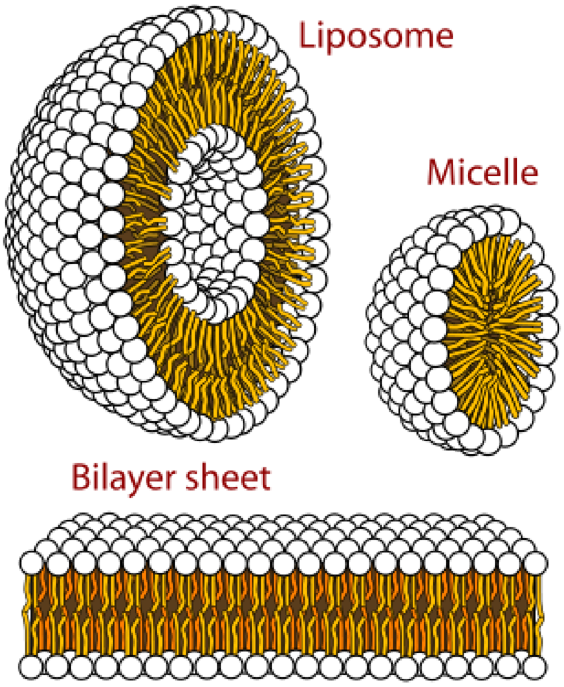

Figure 1.2: Examples for lipid structures in aqueous solutions: lipids arrange in an orientationally ordered way in order to exclusively expose the hydrophilic headgroups to the water environment. Headgroups are shown as white circles, the yellow lines denote the fatty acid chains.[5]

Apart from the structure of their aggregates, there is also a variety of phases that lipids can exhibit, that are mainly distinguished by the behaviour of the tail groups. In the *fluid phase* lipids are free to diffuse within their monolayer without any long range positional order of their tails, but they can also condense into a more ordered *gel phase* below their melting temperature T_m. In aggregates containing more than one lipid species, lipids may also separate into regions of different phases (*domains, rafts*).[6, 7]

1.1.1 Intrinsic curvature and structures

The shape of lipid-aggregates is highly influenced by the individual shapes of their components. The parameter of interest is the *intrinsic* (*spontaneous*) *curvature* C_0. It is defined as the inverse of the radius of an unstressed monolayer formed by a single type of lipid. In case of inverted phases (i.e. headgroups are pointing to the centre) the spontaneous curvature is negative. Curvature is an important parameter in the calculation of surface energies [8] and plays a substantial role in lipid/protein interactions.[9, 10]

The plane, where to measure the monolayer radius is arbitrary in principle. Since C_0 is an important parameter in the calculation of stress due to bending and stretching, we measure it at the neutral plane, where these mechanisms are decoupled.[11] It is assumed to coincide with the position of the lipid backbone R_0 (see figure 1.3).[1]

$$C_0 = -\frac{1}{R_0} \tag{1.1}$$

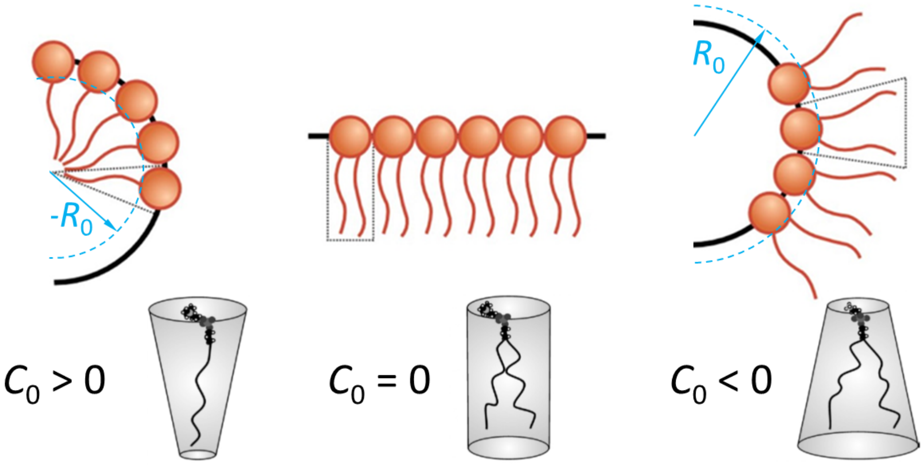

Figure 1.3: Different shapes of lipid molecules, determining the spontaneous curvature of a monolayer.

The spontaneous curvature depends mainly on the size of the headgroup, the number of tails and the degree of unsaturation. Unsaturated chains tend to occupy more space in the lateral direction. A possible structure for lipids of negative spontaneous curvature is the inverted hexagonal phase (H_{II}, figure 1.4). It consists of long cylinders of curled up lipid monolayers, arranged in a 2D-hexagonal lattice. However, using solely lipids, the structure is not stress-free since the cylinders will deform to fill the spaces between them. Adding a filler molecule made of only hydrocarbon chains will let the system adopt a relaxed equilibrium position with the monolayers in their native curvature.[12, 13]

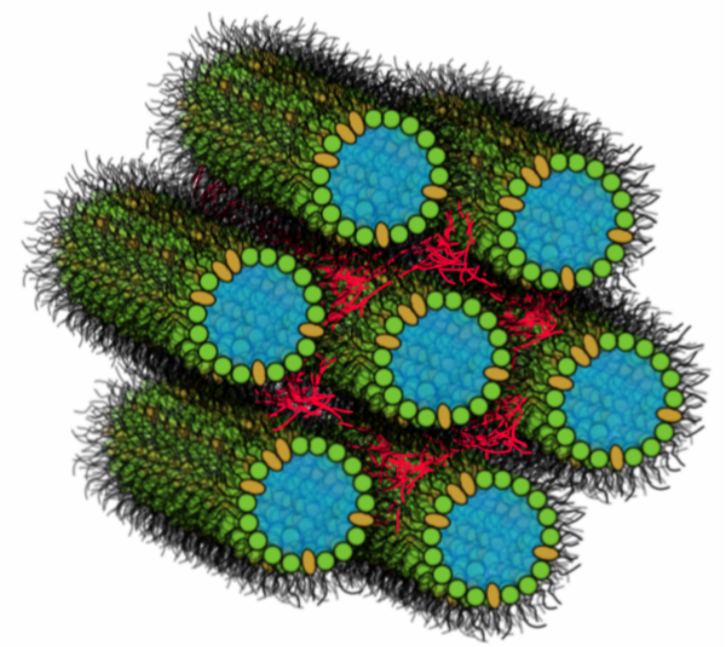

Figure 1.4: Inverted hexagonal phase (H_{II}): Monolayers of different lipid species (green, orange headgroups, black hydrocarbon chains) arrange around water cylinders (blue), forming a 2D hexagonal lattice. The spaces between them are filled with additional hydrocarbon chains (red).

1.1.2 Types of lipids

DOPE

1,2-dioleoyl-sn-glycero-3-phosphoethanolamine (18:1(Δ9-Cis) PE, DOPE) is a glycerophospholipid with the rather small PE-headgroup and two identical unsaturated hydrocarbon chains (18:1). It has a negative spontaneous curvature and a transition temperature from lamellar to inverted hexagonal between 3 and 10 °C ([14], p.770). We will be using DOPE as a *host lipid* for lipid species, which would form different structures in their pure state (*guest lipids*).

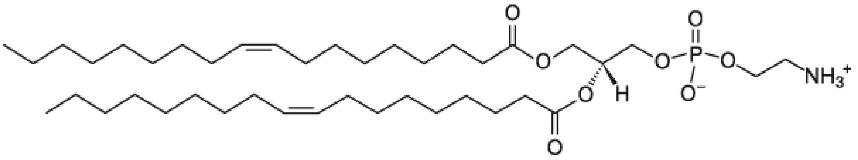

Figure 1.5: Chemical structure of DOPE[15]

Unsaturated glycerophospholipids with a PC-headgroup

1,2-dimyristoyl-sn-glycero-3-phosphocholine (DMPC) and *1,2-dipalmitoyl-sn-glycero-3-phosphocholine* (DPPC) are very similar lipids, distinguished only by the length of their saturated hydrocarbon chains (14:0, 16:0). They are bilayer-forming lipids with a small positive spontaneous curvature. Added to a hexagonal aggregate in small concentrations, they are expected to fit into the layer without disturbing the structure. They have their melting temperatures (transition point from gel to liquid phase) at around 24 °C (DMPC) and 41 °C (DPPC; [14], p.548).

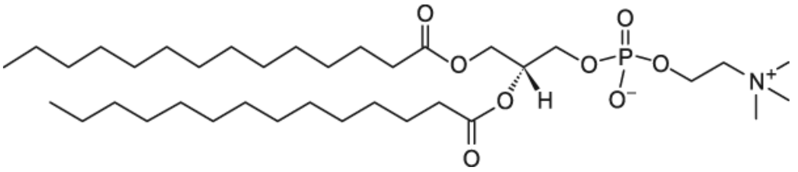

(a) DMPC (14:0)

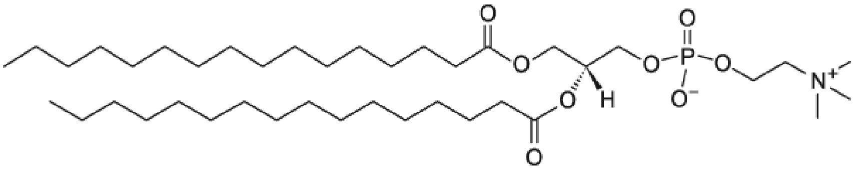

(b) DPPC (16:0)

Figure 1.6: Chemical structures of PC-lipids[15]

Sphingomyelin

Sphingomyelin (SM) is a sphingolipid, which has the same PC-headgroups as the lipids above. Egg-Sphingomyelin, which was used in the experiment, is a natural mixture of lipids of different hydrocarbon chains. The predominant species has a 16:0-tail and a phase transition around 40 °C ([14], p. 577).

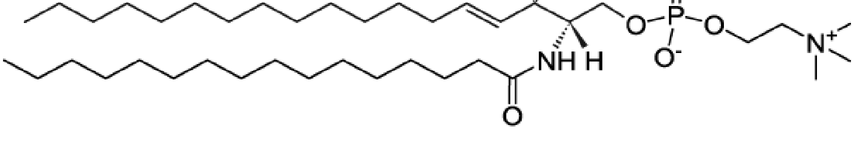

Figure 1.7: Chemical structure of Egg-Sphingomyelin (predominant species)[15]

Filler molecules

(Z)-9-Tricosene is used as a supplement in the experiment to support the structure we are trying to achieve. It consists purely of hydrocarbon chains, including one double bond and is expected to fill the gaps between cylinders in the hexagonal structure, due to its hydrophobic character. In nature it is found as a hormone in house flies.[16]

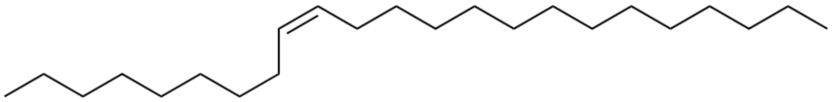

Figure 1.8: Chemical structure of (Z)-9-Tricosene[17]

Another molecule with a similar structure, but a higher number of double bonds, is *Squalene*. As it was shown that double bonds make a molecule more rigid and therefore impede the interdigitation with the lipid tails [12], we are also testing this molecule as a filler in the hexagonal phase. It is a common molecule in all plants and animals.

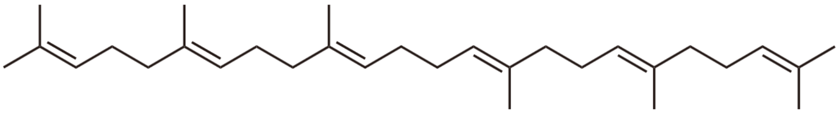

Figure 1.9: Chemical structure of Squalene

Table 1.1: Characteristics of Tricosene and Squalene

Molecule	Chemical formula	Molar mass [g/mol]	No. of double bonds
(Z)-9-Tricosene	$C_{23}H_{46}$	322.62	1
Squalene	$C_{30}H_{50}$	410.71	6

1.2 Small-angle X-ray scattering theory

We consider here the refraction of X-rays passing through soft matter. X-rays are transverse electromagnetic waves, with wavelengths λ around 0.5 to 2.5 Å^{-1}. The velocity in matter is around the same as in vacuum, which indicates that there is almost no refraction. Interactions with matter occur through elastic and inelastic (*Compton*) scattering with electrons and the photoelectric effect.[18] Since we are dealing with structures much larger than the wavelength of the radiation, relevant diffraction peaks will be in a small angle range. In this domain we can neglect all but elastically scattered X-rays.

The binding energies of electrons in light atoms, as present in biological materials, are much smaller than the photon energy of X-rays. We can thus treat them as free electrons and calculate outgoing intensity of the beam by the Thomson formula:

$$I_e(\theta) = I_p \frac{r_e^2}{a^2} \frac{1 + \cos^2 2\theta}{2} \tag{1.2}$$

Here, I_p is the primary intensity, r_e the classical electron radius and a the distance between the scattering event and the detector. The dependence of the scattering angle 2θ is of cos-shape and therefore approximately 1 in the small-angle range.[19] In further calculations we will only be dealing with relative intensities and therefore omit the constant I_e.

1.2.1 Interference

To evaluate the interference pattern of X-rays scattered by the electron cloud of the lipid aggregate, we first consider scattering with single electrons. The incoming and outgoing radiation is coherent, since only elastic scattering is considered. This means that we can add up all amplitudes and calculate the intensity by the absolute square of the resulting amplitude.[19]
We consider scattering at an angle 2θ from two neighbouring points O and P (see fig. 1.10). S_0 and S denote the unitary direction vectors of the incident and the scattered beam. The path difference between upper and lower wave is the distance $\overline{mO} + \overline{On}$, which can be evaluated through simple geometrical considerations to $-(\mathbf{S} - \mathbf{S_0}) \cdot \mathbf{r}$. The phase difference is therefore $\varphi = -\frac{2\pi}{\lambda}(\mathbf{S} - \mathbf{S_0}) \cdot \mathbf{r} = -\mathbf{q} \cdot \mathbf{r}$. We call $\mathbf{q} = \frac{2\pi}{\lambda}(\mathbf{S} - \mathbf{S_0})$ the scattering vector, whose modulus is linked to the scattering angle by $q = \frac{4\pi}{\lambda} \sin\theta$.

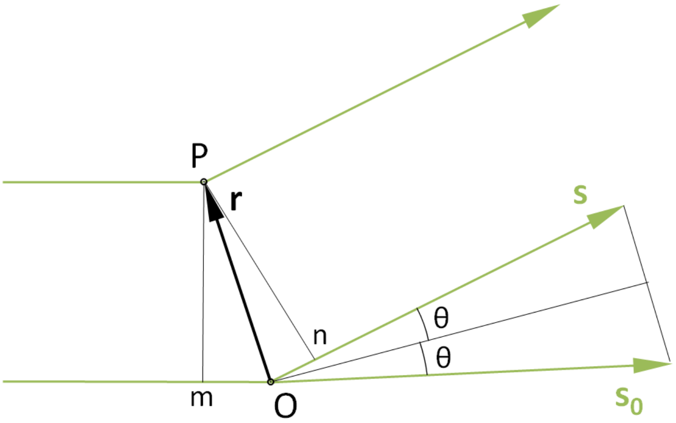

Figure 1.10: Elastic scattering from adjacent scattering centers O and P. S_0 and S denote the primary and the scattered beam.

To get the total amplitude $A(\mathbf{q})$, we have to sum over all scattering centres. However, electrons are not localized. It is therefore necessary to introduce the electron density $\rho(\mathbf{r})$ and integrate the whole irradiated volume:

$$A(\mathbf{q}) = \int dV \ \rho(\mathbf{r})\mathrm{e}^{-i\mathbf{q}\cdot\mathbf{r}} \tag{1.3}$$

1.2.2 Form and structure factor

In the case of a periodic structure, we do not need to integrate over the whole space. We divide the integral into a sum over localized units on positions R_j and integrate over the volume of these units.

$$A(\mathbf{q}) = \sum_{j=1}^{N} \mathrm{e}^{-i\mathbf{q}\cdot\mathbf{R_j}} \int \rho(\mathbf{r_j})\mathrm{e}^{-i\mathbf{q}\cdot\mathbf{r_j}} \ d^3r_j \tag{1.4}$$

If we assume that all units are equal, we can pull the integral out of the sum and in this way factorize the equation:

$$A(\mathbf{q}) = \int \rho(\mathbf{r})\mathrm{e}^{-i\mathbf{q}\cdot\mathbf{r}} \ d^3r * \sum_{j=1}^{N} \mathrm{e}^{-i\mathbf{q}\cdot\mathbf{R_j}} \tag{1.5}$$

The first part of the equation will further be called form factor $F(\mathbf{q}) = \int \rho(\mathbf{r})\mathrm{e}^{-i\mathbf{q}\cdot\mathbf{r}} \ d^3r$. The scattering intensity is proportional to the absolute square of the amplitude:

$$\mathcal{I}(\mathbf{q}) \propto A(\mathbf{q})A^*(\mathbf{q}) = |\int \rho(\mathbf{r})\mathrm{e}^{-i\mathbf{q}\cdot\mathbf{r}} \ d^3r|^2 * \left(1 + \frac{1}{N}\sum_{j\neq k}^{N} \mathrm{e}^{-i\mathbf{q}\cdot(\mathbf{R_j}-\mathbf{R_k})}\right) = |F(\mathbf{q})|^2 * S(\mathbf{q}) \tag{1.6}$$

Here, we introduced the structure factor $S(\mathbf{q})$, where we have split the sum into equal and unequal indices and normalized it by the factor $\frac{1}{N}$.

1.2.3 Thermal displacement

We start at equation (1.5). To include thermal oscillations, we divide $\mathbf{R}_j$ into an average position $\mathbf{R}_{j,0}$ and a time dependent displacement vector $\mathbf{u}_j(t)$. The length of a measurement will be much longer than the oscillation periods, so we can average the amplitude over time:

$$\overline{A(\mathbf{q},t)} = F(\mathbf{q}) \sum_j \overline{\mathrm{e}^{i\mathbf{q}\cdot(\mathbf{R}_{j,0}+\mathbf{u}_j(t))}} = F(\mathbf{q}) \sum_j \mathrm{e}^{i\mathbf{q}\cdot\mathbf{R}_{j,0}} \overline{\mathrm{e}^{i\mathbf{q}\cdot\mathbf{u}_j(t)}} \tag{1.7}$$

Assuming small oscillations, we can express the exponential function as a Taylor series and cut at second order:

$$\overline{\mathrm{e}^{i\mathbf{q}\cdot\mathbf{u}_j(t)}} \approx 1 + i\overline{\mathbf{q}\cdot\mathbf{u}_j(t)} - \frac{1}{2}\overline{(\mathbf{q}\cdot\mathbf{u}_j(t))^2} \tag{1.8}$$

The first order term vanishes, since thermal oscillations in all directions statistically cancel out. We evaluate the scalar product in the second order term to $q^2\overline{|\mathbf{u}_j(t)|^2}\ \overline{\cos^2\alpha(t)}$ and average $\cos^2\alpha$ over the range from 0 to π, which gives $\frac{1}{3}$. Inserting back into the exponential function, we have:

$$\overline{\mathrm{e}^{i\mathbf{q}\cdot\mathbf{u}_j(t)}} \approx 1 - \frac{1}{6}q^2\overline{|\mathbf{u}_j(t)|^2} \approx \mathrm{e}^{-\frac{1}{6}q^2\overline{|\mathbf{u}_j(t)|^2}} \tag{1.9}$$

Since all units are assumed to be the same, we can set $\overline{|\mathbf{u}_j(t)|^2} = \overline{|\mathbf{u}(t)|^2}$ and - inserting in (1.7) - pull it out of the sum. We further rename $\mathbf{R_{j,0}}$ to $\mathbf{R_j}$. The structure factor, including thermal oscillations becomes

$$S(\mathbf{q}) = 1 + \frac{1}{N}\mathrm{e}^{-\frac{1}{3}q^2\overline{|\mathbf{u}(t)|^2}} \sum_{j\neq k}^{N} \mathrm{e}^{-i\mathbf{q}\cdot(\mathbf{R}_j-\mathbf{R}_k)} = 1 + \frac{1}{N}\mathrm{e}^{-q^2\Delta} \sum_{j\neq k}^{N} \mathrm{e}^{-i\mathbf{q}\cdot(\mathbf{R}_j-\mathbf{R}_k)} \tag{1.10}$$

Here we introduced the temperature dependent thermal displacement parameter $\Delta = \frac{1}{3}\overline{|\mathbf{u}(t)|^2}$.

1.2.4 Cylinder aggregates

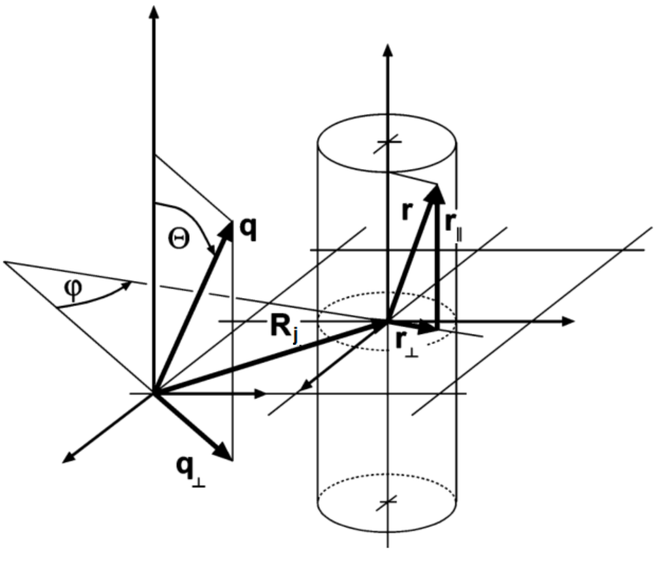

Figure 1.11: Parametrisation of the cylindrical unit.[20]

We parametrize the structure as shown in figure 1.11. Carrying out the scalar product in the exponent of (1.2.3) and averaging over all angles φ, we get to a form including the 0th order Bessel function J_0:

$$S(q,\theta) = 1 + \frac{1}{N}\mathrm{e}^{-q^2\Delta}\sum_{j\neq k}^{N} J_0(q|\mathbf{R}_j - \mathbf{R}_k|\sin\theta) \tag{1.11}$$

At last, we want to write out the integration necessary for the form factor. We assume the electron density to be homogeneous along the rotational axes of the cylinder as well as rotationally symmetric. The integral to be evaluated is

$$F(q,\theta) = \int_{-\frac{L}{2}}^{-\frac{L}{2}} \mathrm{e}^{iqr_\parallel\cos\theta} dr_\parallel \int_0^R r_\perp\rho(r_\perp)\int_0^{2\pi} \mathrm{e}^{iqr_\perp\cos\varphi\sin\theta} d\varphi\ dr_\perp \tag{1.12}$$

where R is the outer radius and L the length of the cylinder. The formula can be simplifed by integrating to:

$$F(q,\theta) = \frac{4\pi\sin(\frac{L}{2}q\cos\theta)}{q\cos\theta}\int_0^R r_\perp\rho(r_\perp)J_0(qr_\perp\sin\theta)dr_\perp \tag{1.13}$$

The total intensity, depending only on the modulus of the scattering vector, is obtained by averaging over θ:

$$\mathcal{I}(q) \propto \int_0^\pi |F(q,\theta)|^2 S(q,\theta)\sin\theta d\theta \tag{1.14}$$

1.2.5 Bilayer form factor and cross-term

Due to reasons discussed in chapter .., it is also necessary to include a bilayer form factor into the model. Its derivation is done similarly to the cylinder. We work in cartesian coordinates with an electron density changing only in one direction. From (1.3) follows:

$$A_{BL}(\mathbf{q}) = \int \mathrm{e}^{-iq_x\cdot x}\ dx \int \mathrm{e}^{-iq_y\cdot y}\ dy \int \rho(z)\mathrm{e}^{-iq_z\cdot z}\ dz = 4\pi^2\delta(q_x)\delta(q_y)\int\rho(z)\mathrm{e}^{-iq_z\cdot z}\ dz \tag{1.15}$$

The first two integrals, evaluated from $-\infty$ to ∞, each yield a Dirac delta function. Averaging over all orientations as before, will only give results if $q_z = q$. Thus, we have acquired the bilayer form factor:

$$F_{BL}(q) = 4\pi^2\int\rho(z)\mathrm{e}^{-iq_z\cdot z}\ dz \tag{1.16}$$

In a sample consisting of hexagonal as well as layered structures, we can add up the scattering amplitudes of both contributions. We get an expression for the total intensity:

$$\begin{aligned}\mathcal{I}(q) \propto \int_0^\pi |F(q,\theta)|^2 S(q,\theta)\sin\theta d\theta\ +\ F_{BL}(q)\int_0^\pi F(q,\theta)s(q,\theta)\sin\theta d\theta\ +\\ +\ P^*_{BL}(q)\int_0^\pi F^*(q,\theta)s^*(q,\theta)\sin\theta d\theta\ +\ |F_{BL}(q)|^2\end{aligned} \tag{1.17}$$

Or, in the case of a center of symmetry (i.e. all imaginary parts vanish):

$$\mathcal{I}(q) \propto \int_0^\pi |F(q,\theta)|^2 S(q,\theta)\sin\theta d\theta\ +\ 2F_{BL}(q)\int_0^\pi F(q,\theta)s(q,\theta)\sin\theta d\theta\ +\ |F_{BL}(q)|^2 \tag{1.18}$$

$s(q,\theta)$, which occurs in the cross-term, is acquired analogously as the structure factor and is given by:

$$s(q,\theta) = \frac{1}{\sqrt{N}}\mathrm{e}^{-q^2\Delta/2}\sum_{j}^{N} J_0(q|\mathbf{R}_j|\sin\theta) \tag{1.19}$$

2 Methods

In this work we tried to develop a new method consisting of experimental and theoretical work. Both parts have not been optimized for the current problem and here we are mainly focussed on the theoretical part. In the experimental section the current way of sample preparation is described, but a standardized method is still to determine.

2.1 Experimental techniques

2.1.1 Sample preparation

Sample preparation was done by the Rapid Solvent Exchange (RSE) method.[21, 22, 2] Lipids were purchased by Avanti Polar Lipids (Alabaster, AL) in powder form.
6 mg lipid (or combination of lipids) was dissolved in a chloroform/methanol 9:1-mixture with a concentration of 10 mg/ml (The concentration was lowered in comparison to [2] for better pipetting accuracy.). Different lipid species were dissolved in separate recipients. For the filler molecule the same solvent was used, but a concentration of 5 mg/ml. 0.3 ml water (ultra pure, 18 mOhm) was pre-heated to a temperature of 60 to 70 °C. The dissolved lipids and filler was added to the water and immediately inserted into the RSE-apparatus (see figure 2.1). In the machine, the sample was simultaneously heated to 65 °C, vortexed at 600 rpm (The velocity was reduced in comparison to [2] to avoid that the sample raises up the glass wall and sticks to it.) and exposed to a vacuum of 400 to 500 mBar and to a Argon flow of 60 ml/min. This process was continued until all solvent was evaporated (approx. 5 min).

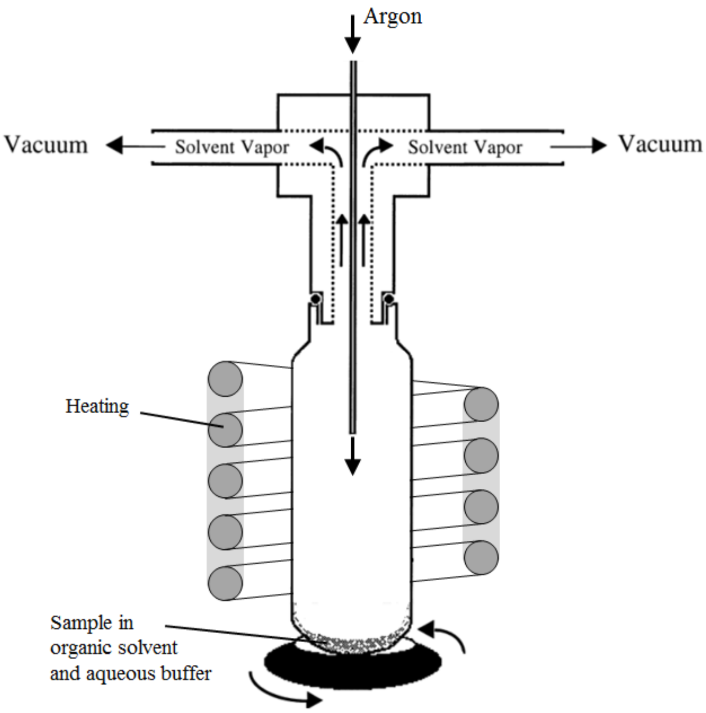

Figure 2.1: Schematic representation of the RSE-apparatus.[21]

Samples marked by * in tables 3.1 and 3.4 were prepared using the parameters above. Samples marked by ** used: temperature: 45 °C, pressure: 200 mbar, vortex speed: 1800 rpm, Argon flow: 61 ml/min [2].

Table 2.1: Pure samples prepared by the RSE-method.
* and ** denote different peparation parameters (see section 2.1.1)

No.	Host lipid	Filler molecule	wt%	Note
1	DOPE	none		*
2	DOPE	Tricosene	10	*
3a	DOPE	Tricosene	12	prepared by M. Pachler*
3b	DOPE	Tricosene	12	prepared by N. Negahbani**
4	DOPE	Squalene	9	*
5	DOPE	Squalene	12	*
6	DOPE	Squalene	13	*
7	DOPE	Squalene	14	*
8	DOPE	Squalene	15	*
9	DMPE	Tricosene	12	prepared by M. Pachler*

Table 2.2: Mixed samples prepared by the RSE-method. In all samples 12 wt% tricosene was used as filler.
and ** denote different peparation parameters (see section 2.1.1)

No.	Host lipid	Guest lipid	mol%	Note
M1	DOPE	DMPC	10	prepared by N. Negahbani**
M2	DOPE	DMPC	20	prepared by N. Negahbani**
M3	DOPE	DPPC	10	prepared by N. Negahbani**
M4	DOPE	DPPC	20	prepared by N. Negahbani**
M5	DOPE	DPPC	30	prepared by N. Negahbani**
M6	DOPE	DLPE	10	prepared by M. Pachler*
M7	DOPE	DLPE	20	prepared by M. Pachler*
M8	DOPE	Egg-Sphingomyelin (SM)	10	prepared by N. Negahbani**
M9	DOPE	Egg-Sphingomyelin (SM)	20	prepared by N. Negahbani**

2.1.2 Polarized light microscopy

This method was used to get an overview of the sample structure. It is a simple optical microscopy technique, making use of the optical path difference of light after traveling through a birefringent material. If a heterogeneous sample with birefringent regions is irradiated by polarized light, one can achieve different contrasts by adjusting the angle of an analyzer placed behind the sample. If the analyzer angle matches the rotation caused by the sample, only the birefringent parts appear white in the image.

2.1.3 Small angle X-ray scattering

Small angle X-ray scattering (SAXS, figure 2.2) experiments were done at the *University of Graz*, using an X-ray tube with Cu Kα (1.54 Å) radiation (device: *SAXSpace* by *Anton Paar GmbH*, Graz) and a Eiger R 1M detector system (Dectris, Switzerland). Samples were measured in a paste cell (*Anton Paar*) at a sample to detector distance (*SDD*) of 308 mm and exposed to the beam in 4 frames of 8 min per measurement. The sample temperature was regulated by the TC Stage 150 (*Anton Paar*). Data reduction, distance to q-conversion, normalization and background subtraction were done by the *Anton Paar*-software *SAXSanalysis*.

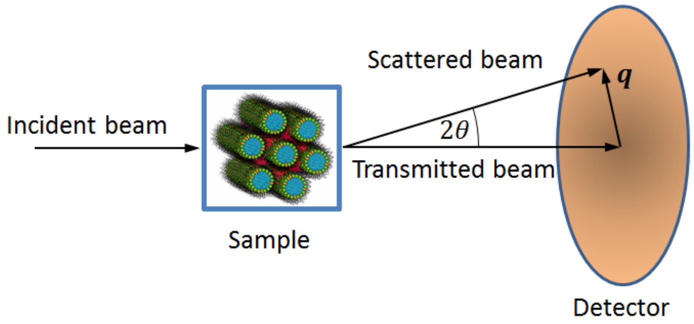

Figure 2.2: Schematic representation of the SAXS-experiment.

2.2 Scattering data evaluation

2.2.1 Model-free approach

To extract the scattering length density profile from the SAXS-spectrum, without any prior assumptions except the presence of a hexagonal lattice, we attempted to perform a generalized inverse Fourier transformation.[23, 20] This was done in cooperation with Otto Glatter. We shall forestall here that this method provided perfect fits to the data, but no physically meaningful results. This indicates the necessity of modelling as well as the presence of no purely hexagonal phase.

2.2.2 Modelling of the hexagonal lattice

We imagine a bundle of cylinders consisting of a water core covered by lipids, as illustrated in figure 1.4. The spaces between the cylinders are occupied by the filler molecule. To calculate the structure factor, we need to obtain the distances between the cylinders. We define a lattice as shown in figure 2.3, determined by its lattice parameter a and the number of rings (lattice order n).

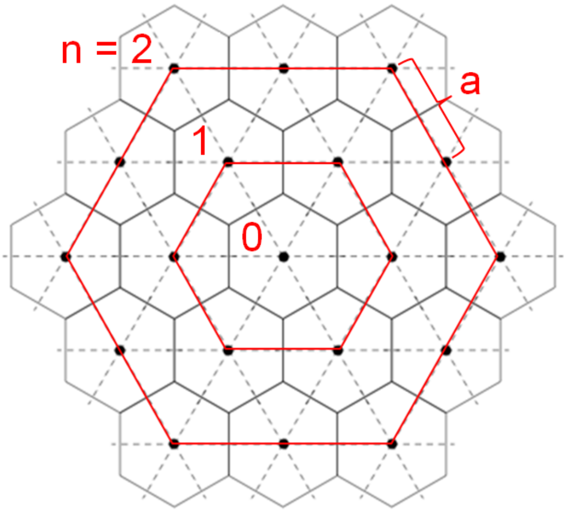

Figure 2.3: Hexagonal lattice. n denotes the lattice order, a the lattice parameter.

The diameter of an aggregate is approximately

$$D = (2n + 1) * a, \tag{2.1}$$

Computing the term $\frac{1}{N}\sum_{j\neq k}^{N} J_0(q|\mathbf{R}_j - \mathbf{R}_k|\sin\theta)$ in the structure factor is rather expensive due to the nature of the Bessel function. To facilitate an efficient computation in a routine of many consecutive calculations, we pre-calculate it for a range of lattice orders which are eligible for the data. The lattice parameter is well defined by the peak positions, which are located at

$$q_{hk} = \frac{4\pi}{a\sqrt{3}}\sqrt{h^2 + hk + k^2};\ \ h, k = 0, 1, 2, ... \tag{2.2}$$

In contrast to this rather straightforward model, we tested an empirical model published by Förster et al.[24] This *Multiple Peak Model* although contains a higher number of parameters and yielded no advantage in comparison to the cylinder bundle model.

2.2.3 Lipid unit cell and form factor

The next step is designing the cylinders within the lattice. Their length is supposed to be much longer than their diameter. Evaluating the prefactor of the form factor integral $f(q,\theta) = \frac{4\pi\sin(\frac{L}{2}q\cos\theta)}{q\cos\theta}$, we find that if L is above some threshold, the function is rather independent of L. However, with higher values of L, the sin-term oscillates faster, thus more sampling points of θ are needed. We found 2500 Å to be a convenient value for calculations. Hence, we can evaluate this factor in advance.

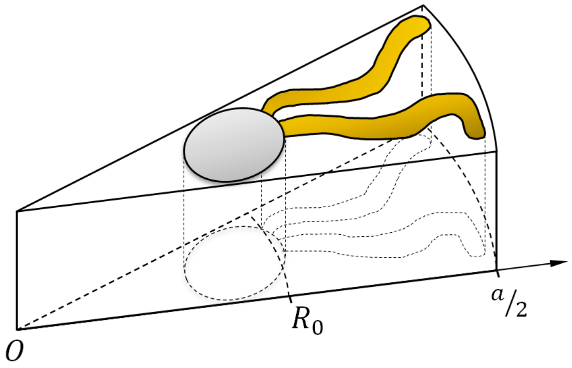

Figure 2.4: Lipid unit cell in the hexagonal phase. The outer radius is half the lattice parameter a. The backbone of the lipid is located at the radius R_0.

The rest of the form factor is determined by the radial electron density profile. We determine it by filling a lipid molecule into its unit cell, which has the shape of a cylinder sector, as shown in figure 2.4.

We split the lipid into 3 parts of different electron densities: head, backbone and tail (see figure 2.5). Treating the backbone separately is necessary to locate the position of the neutral plane.

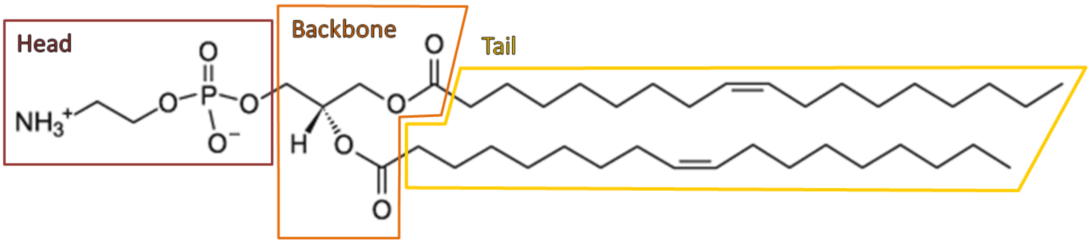

Figure 2.5: Subdivision of a lipid molecule into head, backbone and tail using the example of DOPE.

The volume of a slab in the unit cell of height h and opening angle α, limited by an inner and an outer radius (r_i, r_o) is given by

$$V_{slab}(r_i, r_o) = \frac{\alpha h(r_o^2 - r_i^2)}{2} = \frac{\hat{A}/\hat{r}(r_o^2 - r_i^2)}{2} \tag{2.3}$$

We introduced the unit area $\hat{A}$, which is the mantle area of the cylinder sector at a unitary radius $\hat{r}$. The volume which the hydrocarbon chains occupy is $V_{slab}(R_0 + d_{BB}/2, a/2)$, where d_{BB} is the backbone width. Using this, we can calculate $\hat{A}$ and determine the volumes of the headgroup slabs. The number of water molecules in the backbone-slab is then given by $[V_{slab}(R_0 - d_{BB}/2, R_0 + d_{BB}/2) - V_{BB}]/V_{H_2O}$ and analogously for the head-slab. Then we count the electrons and calculate the electron density in each slab. The radial electron density profile with N slabs is given by:

$$\Delta\rho_e(r) = \rho_e(r) - \rho_{e,H_2O} = \sum_{k=1}^{N} \Delta\rho_{e,k} \left[\Theta(r - r_{i,k}) - \Theta(r - r_{o,k})\right] \tag{2.4}$$

Of course $r_{o,k} \equiv r_{i,k+1}$.

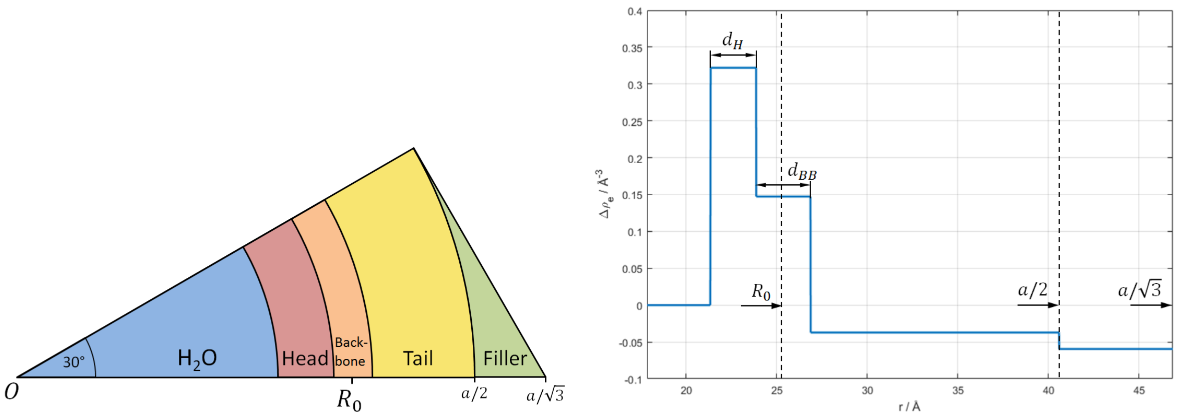

Figure 2.6: Left side: Illustration of the area which needs to be integrated in the unit cell.
Right side: Examplary electron density profile.

In figure 2.6 to the left we see a twelfth the area over which we have to integrate. For the cylinder until $a/2$ we can evaluate the integral in (1.2.4) analytically and get the result

$$\begin{aligned} F_{lipid}(q, \theta; \{r_{o,k}\}, \{\Delta\rho_{e,k}\}) &= f(q,\theta) \int_0^{a/2} r\Delta\rho_e(r) J_0(qr\sin\theta) dr = \\ &= \frac{f(q,\theta)}{q\sin\theta} [\Delta\rho_{e,N} r_{o,N} J_1(qr_{o,N}\sin\theta) + \sum_{k=1}^{N-1} (\Delta\rho_{e,k} - \Delta\rho_{e,k+1}) r_{o,k} J_1(qr_{o,k}\sin\theta)] \end{aligned} \tag{2.5}$$

The rest of the integral (filler) is integrated numerically and also pre-calculated within fitting-algorithms. It is given by

$$F_{filler}(q,\theta) = \frac{f(q,\theta)}{2\pi} * 12 \int_0^{\pi/6} \int_{a/2}^{\frac{a}{2\cos(\varphi)}} r\Delta\rho_{e,filler} J_0(qr\sin\theta) dr d\varphi \tag{2.6}$$

For the total form factor we add F_{lipid} and F_{filler}.

2.2.4 Lipid fluctuations and scaling parameters

The facilitate a lift-off of the form factor minima, we allow the lipids to fluctuate to the in- and outside of the cylinder. Therefore we sum over a couple of form factors, which contain unit cells that are radially shifted by a distance x_i and weighed by a Gaussian distribution $\mathcal{N}(x|0,\sigma^2_{fluc})$ with mean 0 and variance σ^2_{fluc}.

$$F_{lipid,fluc}(q,\theta) = \sum_i \mathcal{N}(x_i|0,\sigma^2_{fluc})\ F_{lipid}(q,\theta;\{r_{o,k}\}+x_i,\{\Delta\rho_{e,k}\}) \tag{2.7}$$

To complete the model for single lipid aggregates, we introduce 2 more parameters:
λ_0 is a constant, additive background which could be caused by local fluctuations within the molecule groups. It mainly causes a lift-off in the high-q region where the form factor decays to very small values.
λ_1 is a scaling constant, adapting the total fitting curve to the height of the spectrum which is arbitrary in principles. Thus, this constant has no physical meaning.
This transformation is performed at the end of the calculation:

$$\mathcal{I}(q) \to \lambda_1 \mathcal{I}(q) + \lambda_0 \tag{2.8}$$

2.2.5 Addition of curvature in binary lipid mixtures

As we add a small amount of a second lipid species (*guest*), these are expected to incorporate into the hexagonal phase and uniformly spread within the aggregate. Guest lipids with different shape will change the cylinder radius according to their curvature. However, the exact mechanism of curvature addition is still unclear. In former calculations, usually a linear addition of curvatures was assumed [25, 1]:

$$C_0 = (1-x)C_{0,host} + xC_{0,guest} \tag{2.9}$$

where

$$x = \frac{N_B}{N_A + N_B} \tag{2.10}$$

is the mole fraction (i.e., the number concentration) of component B.

The following considerations about non-linear curvature addition originate in an unpublished work by Primož Ziherl:
We consider a two-component mixture consisting of lipids characterized by wedge angles ω_A and ω_B and headgroup areas a_A and a_B measured in the neutral plane. Since the location of the neutral plane in a mixture need not be the same as in a pure monolayer, a_A and a_B are to some extent adjustable parameters, possibly even dependent on concentration. For present purposes, it is important to appreciate that a_A and a_B are generally different. We assume that (i) the lipids mix at all concentrations, that (ii) the mixture forms the inverted cylindrical micelle phase $\mathrm{H_{II}}$ and so that the shape of both components is a truncated wedge, and that (iii) the dimension of the headgroup along the micelle is the same in both components. Thus each of the two components can be characterized by its effective in-plane dimension in the neutral plane, which is often close to the glycerol backbone of phospholipids [1] In figure 2.7, these dimensions are denoted by b_A and b_B for component A and B, respectively.

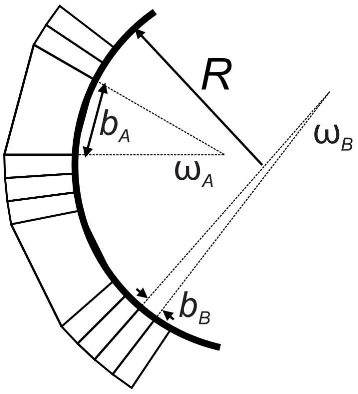

Figure 2.7: Schematic of the cross-section of an inverted cylindrical monolayer micelle consisting of two types of wedge-shaped lipids of angles ω_A and ω_B, respectively, and effective in-plane headgroup dimensions b_A and b_B, respectively. The thick circular arc represents the neutral plane, its radius being R. For simplicity, both components are drawn such that their tail lengths are the same.

In an inverted cylindrical micelle, the total angle of the neutral plane contour seen in the cross-section is 2π, and this angle consists of individual contributions of N_A molecules of type A and N_B molecules of type B (Fig. 2.7):

$$2\pi = N_A\omega_A + N_B\omega_B = (N_A + N_B)[(1-x)\omega_A + x\omega_B]. \tag{2.11}$$

In this notation, positive angles ω_A and ω_B correspond to lipids with a negative curvature and vice versa. Our argument applies both to mixtures where both components have a negative curvature and to those where one component (say B) has a positive curvature as long as the mixture still forms an inverted micelle, that is for N_B small enough so that $2\pi = N_A\omega_A + N_B\omega_B$ holds although $\omega_B < 0$. This condition is fulfilled for $x < x_c = \omega_A/(\omega_A - \omega_B)$. (For $\omega_B \geq 0$, $x_c \geq 1$ and the restriction does not apply.)
The perimeter of the micelle cross-section is

$$P = N_A b_A + N_B b_B = (N_A + N_B)[(1-x)b_A + x b_B], \tag{2.12}$$

where R is the radius of the micelle, and b_A and b_B are the in-plane dimensions of headgroups in component A and B. Now from eq. (2.11) we have $N_A + N_B = 2\pi/[(1-x)\omega_A + x\omega_B]$ so that eq. (2.12) can be rewritten as

$$2\pi R = 2\pi \frac{(1-x)b_A + x b_B}{(1-x)\omega_A + x\omega_B}, \tag{2.13}$$

which implies that the micelle curvature

$$C_0 = -\frac{1}{R_0} = -\frac{(1-x)\omega_A + x\omega_B}{(1-x)b_A + x b_B}, \tag{2.14}$$

(Note that the curvature of inverted micelles is negative, hence the minus sign.) Geometrically, the inplane spontaneous curvature of component A is given by $J_A = -\omega_A/b_A$ and similarly $J_B = -\omega_B/b_B$ for component B; here we took into account that the curvature of inverted-cone lipids which form inverted micelles is negative itself. Thus

$$C_0(b_B/b_A, x) = \frac{(1-x)C_{0,A} + x\frac{b_B}{b_A}C_{0,B}}{(1-x) + x\frac{b_B}{b_A}}. \tag{2.15}$$

This result is valid for all $C_0(b_B/b_A, x) < 0$ where the mixture indeed forms an inverted micelle. For $b_B/b_A = 1$ eq. (2.15) reduces to the linear relationship, eq. (2.9).

2.2.6 Electron density in binary mixtures

To calculate the electron density of the lipid mixture, we need to define a new unit cell. We introduce a hybrid lipid composed of a fraction $(1-x)$ of the host lipid and x of the guest lipid. A hybrid unit cell of a host lipid with a cylindrical guest lipid of equal fractions is shown in figure 2.8.

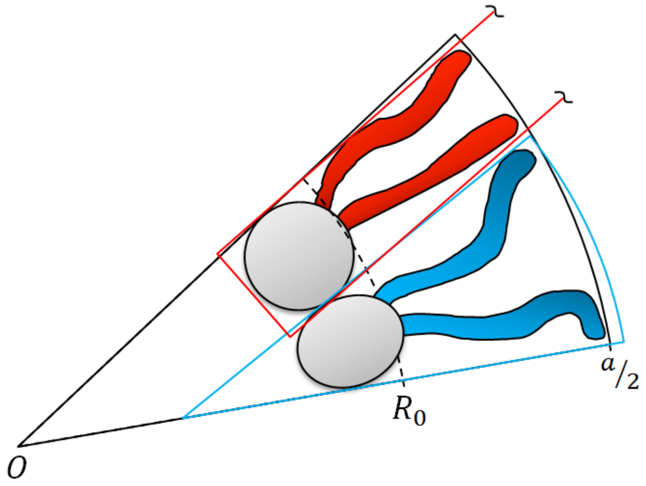

Figure 2.8: Hybrid unit cell of a binary lipid mixture of equal shares. The lipids are aligned at the oil-water interface.

Assuming that the lipids align at the oil-water interface, we can calculate $\hat{A}$ as before using (2.3) and that the hydrocarbon chain volumes are additive:

$$V_{HC} = (1-x)V_{HC,host} + xV_{HC,guest} \tag{2.16}$$

To calculate the factor b_B/b_A, we assume that the projected lateral area per lipid has a quadratic profile at the interface and that the areas $A_{if,i}$ at the interface are additive just as the chain volumes. Using $A_{if} = \hat{A}/\hat{r} \cdot R_0$, we get

$$\frac{b_{guest}}{b_{host}} = \sqrt{\frac{A_{if,guest}}{A_{if,host}}} = \sqrt{\frac{\frac{2V_{HC}}{\frac{a^2}{4}+\frac{1}{C_0}}\left(-\frac{1}{C_0}\right) - (1-x)A_{if,host}}{xA_{if,host}}} \tag{2.17}$$

$A_{if,host}$ is determined from a global SAXS analysis of the host system in the absence of guest lipids. The determined b_{guest}/b_{host} values are consequently inserted into (2.15) and solved for C_0 numerically to acquire the interfacial radius. Then again we can define slabs for all molecule groups and fill them with the respective volumes and electrons. An exemplary hybrid lipid electron density is shown in figure 2.9.

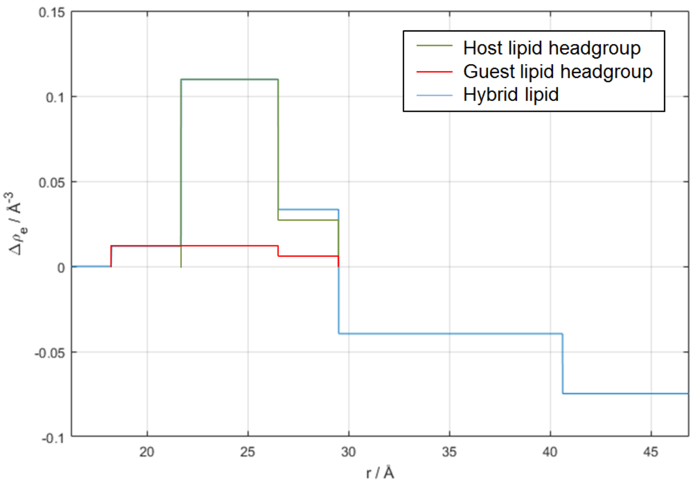

Figure 2.9: Electron density of a hybrid lipid with a small percentage of guest lipid.

2.3 Computational techniques

2.3.1 Differential evolution

Differential evolution (DE) is an evolutionary fit algorithm, which works via creation of random populations of parameter sets, mutation of the individual parameters, crossover with the existing set and selection of the set with the best cost function.[26] It is supposed to be an efficient algorithm, which is robust against local minima because of its mutation and crossover routine. Parameters that determine its functionality are the population size, a mutation constant $F \in [0, 2]$ and a crossover constant $CR \in [0, 1]$. F and CR can be tuned for the existing problem, to reach a good balance between convergence speed and precision.

2.3.2 Markov chain Monte Carlo

Markov chain Monte Carlo (MCMC) sampling is a method to obtain probability distributions, based on Bayesian probability theory (for all derivations of this chapter, see [27]). As a cost function in the algorithm serves the posterior probability $p(\{x_i\}|\mathbf{d}, \sigma, I)$ of the proposed parameter set $\{x_i\}$. It is defined as the probability of a parameter set given the measured data vector $\mathbf{d}$, their errors σ and general information about the system I. According to Bayes' theorem it is the product of prior $p(\{x_i\}|I)$ (information about the parameters, available before doing the experiment) and likelihood function $p(\mathbf{d}|\{x_i\}, \sigma, I)$ (probability of measuring the data, given a parameter set). Since we assume every data point to be an independent event, their joint probability is given by their product. For N data points Bayes' theorem becomes

$$p(\{x_i\}|\mathbf{d}, \sigma, I) = \frac{p(\{x_i\}|I) \prod_{j=1}^{N_{par}} p(d_j|\{x_i\}, \sigma, I)}{Z} \tag{2.18}$$

The variable Z, a normalization constant called evidence, is of no importance in our case. As we are dealing with a counting experiment, experimental errors are in general Poisson distributed. For counting rates > 100 the Poisson distribution is practically indistinguishable to a normal distribution, thus we assume normal distributed errors for the likelihood function. If $\mathcal{I}(q_j, \{x_i\})$ is the function that should resemble the data, the likelihood for a data point d_j is

$$p(d_j|\{x_i\}, \sigma_j, I) = \frac{1}{\sigma_j\sqrt{2\pi}} \exp\left(-\frac{1}{2\sigma_j}(\mathcal{I}(q_j, \{x_i\}) - d_j)^2\right) \tag{2.19}$$

As priors for the parameters we assume uniform distributions between lower and upper borders x_i^l, x_i^u, determined by physics and former measurements. Their normalizations would be the reciprocal value of the sampling range, but since priors are unchanged for every iteration, also these are unimportant for the method.
For reasons of usability we introduced a scaling factor η for the errors given by the X-ray device and perform the transformation $\sigma \rightarrow \eta\sigma$. This gives the code the ability to move through parameter space regions of poor agreement and gives an estimate for the true experimental errors. Here, we use Jeffreys prior $1/\eta$, which assumes scaling invariance.[28] The algorithm is implemented as follows:

1. Start at an arbitrary location $\{x_i^0\}$ in the parameter space.
2. Propose update for a randomly chosen parameter $x_i^T = x_i^0 + 2s_i\ (\mathcal{U}[0,1] - 1/2)$
   Here s_i denotes the stepsize for parameter x_i and $\mathcal{U}[0,1]$ is a random number between 0 and 1, drawn from a uniform distribution.
3. If $x_i^l \geq x_i^T \geq x_i^u$
   Accept if $p(\{x_i^T\}) > p(\{x_i^0\})$
   else generate u from $\mathcal{U}[0,1]$
   accept if $\frac{p(\{x_i^T\})}{p(\{x_i^0\})} > u$
   if accepted: $x_i^0 := x_i^T$
4. repeat from 2.

Parameters samples are saved after every sweep (sweepsize ≈ 1.5 times the number of parameters n_{par} in iterations), to avoid heavily correlated samples (*chain thinning*). Since the first samples might be chosen randomly, they might be far away from the distribution. Therefore, the first 20 % of the samples are not included in the results (*burn-in* phase). Stepsizes are calibrated beforehand for every parameter, so that the acceptance rate lies approximately between 0.5 and 0.8. The code was implemented in Matlab 2016b.
The acquired samples represent a probability density cloud in a n_{par}-dimensional space. From the we calculate the probability distributions (*marginal posterior probabilities*) for each parameter, which have defined mean values and standard deviations. Marginal posteriors are defined as integrals of the posterior $p(\{x_i\}|\mathbf{d}, \sigma, I)$ over all parameters except the ones of interest. This can result in distributions of arbitrary numbers of dimensions, whereby 1 and 2-dimensional are the most demonstrative ones. In the case of MCMC-samples, the integration is replaced by the creation of histograms of all values of the desired parameters. All other parameter values do not have to be considered (they are *marginalized out*). Mean value $\bar{x_i}$ and variance σ_i^2 for a Monte Carlo run of N_{MC} sweeps:

$$\bar{x_i} = \frac{1}{N_{MC}} \sum_{k=1}^{N_{MC}} x_i^k, \quad \sigma_i^2 = \frac{1}{N_{MC}} \sum_{k=1}^{N_{MC}} (x_i^k)^2 - \bar{x_i}^2 \tag{2.20}$$

Since MCMC is basically an educated random walk, new sampling points depend heavily on the position of the prior ones. In addition to the chain thinning, we want to make sure that the number of samples is at least 2 or 3 orders of magnitude larger than the *integrated autocorrelation time* τ. It can be evaluated from the *autocorrelation function* $\rho(j)$, which is a measure for correlations of point that are j Monte Carlo-sweeps apart (usually decaying exponentially with $(-j/\tau)$). For a parameter x, $\rho(j)$ and τ are calculated as follows:

$$\rho(j) = \frac{\Sigma_t \left[(x^{(t)} - \bar{x})(x^{(t+j)} - \bar{x})\right]}{\sqrt{\Sigma_t (x^{(t)} - \bar{x})^2}\sqrt{\Sigma_t (x^{(t+j)} - \bar{x})^2}} \tag{2.21}$$

$$\tau = \frac{1}{2} + \Sigma_j \rho(j) \tag{2.22}$$

3 Results

3.1 Qualitative analysis of the samples

Sample appearance

The samples, coming out of the RSE-apparatus, have usually the form of small, white pellets distributed over the water surface, with small amounts floating in the water and attached to the walls. They are very sticky and can easily be combined to one pellet. The surface does not seem to repel water as one would expect from the outward pointing hydrocarbon chains in a pure inverted phase.

Polarization microscopy

Images from polarization microscopy (figure 3.1) allow a rough estimation of the aggregate sizes. The hexagonal aggregates are birefringent as seen in the polarized images and show accumulations of long, aligned aggregates (concentrated at the edges, as seen in the lower rows of figure 3.1). The images resemble formerly taken ones ([29]).

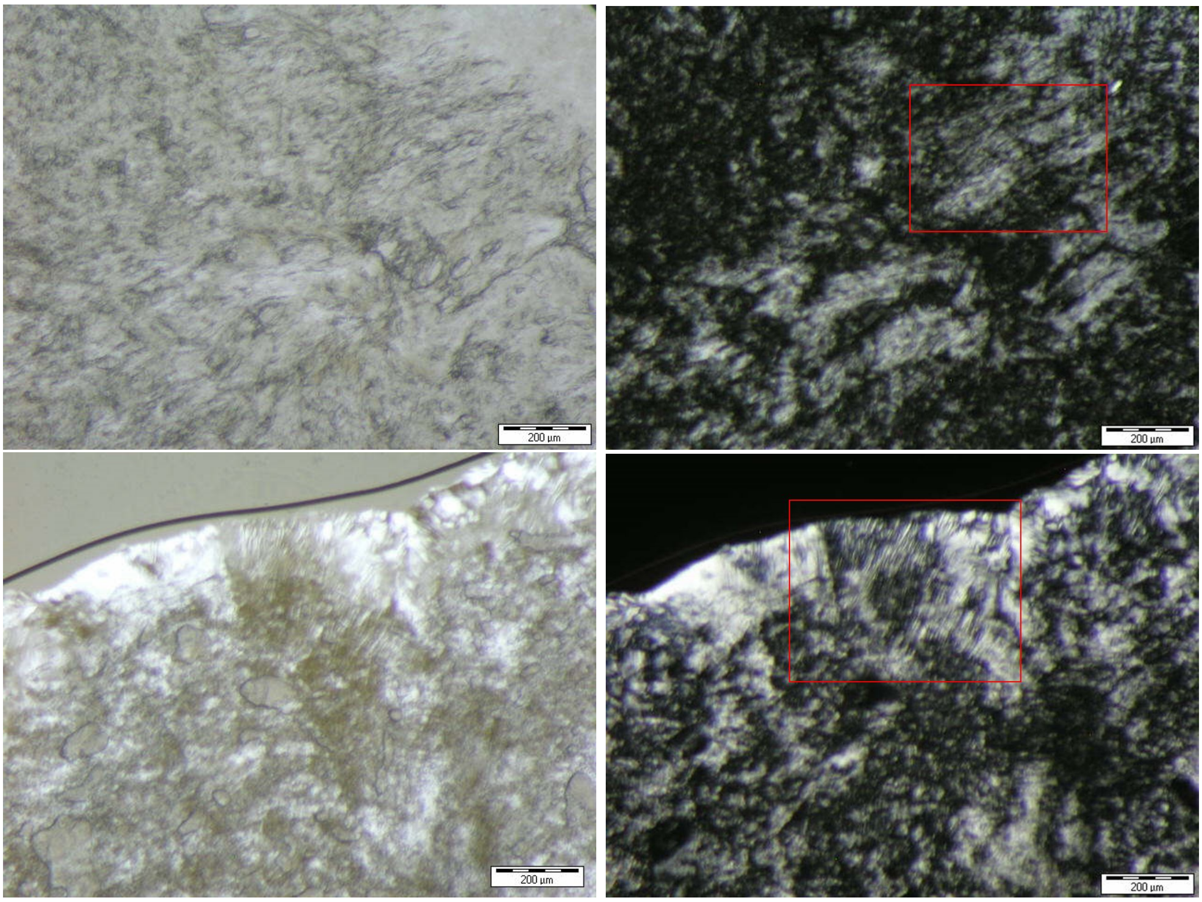

Figure 3.1: Appearance of the samples through a polarisation microscope.
Left side: unpolarized images, right side: polarized to maximum contrast.
Upper row: DOPE + 12% tricosene, lower row: DOPE + 12% squalene

From the details shown in figure 3.2 one can estimate the aggregate diameter to be in the order of a few micrometers and the length in the order of 100 µm.

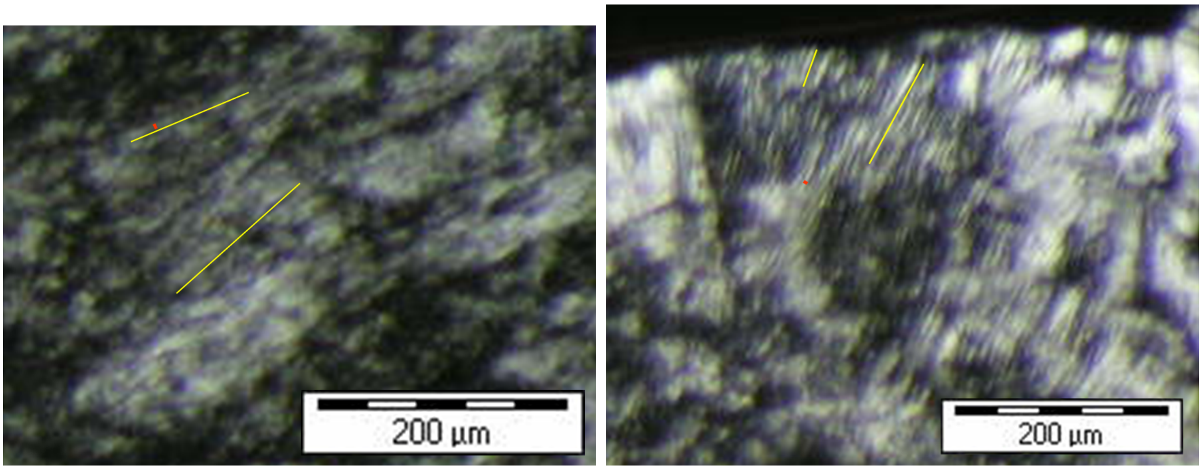

Figure 3.2: Details from the microscope images (red frames from figure 3.1) with marked aggregate diameters (red) and lengths (green).
Left side: DOPE + 12% tricosene, right side: DOPE + 12% squalene

X-ray scattering data

Figure 3.3 shows exemplary data from SAXS-measurements of samples of one lipid. The left spectrum is representative for successful preparations. One can easily recognize the first 7 diffraction peaks, as marked in the figure, whereby the disappearance of the (2,1)-peak is a recurring detail. The right image shows the spectrum of a sample using a too high amount of filler molecule. Additional details around the (1,0)-peak are characteristic for these samples (samples 5, 6, 7).
Deviations from the desired shape were also observed for DOPE above 60 °C, as well as for DMPE below 80 °C.

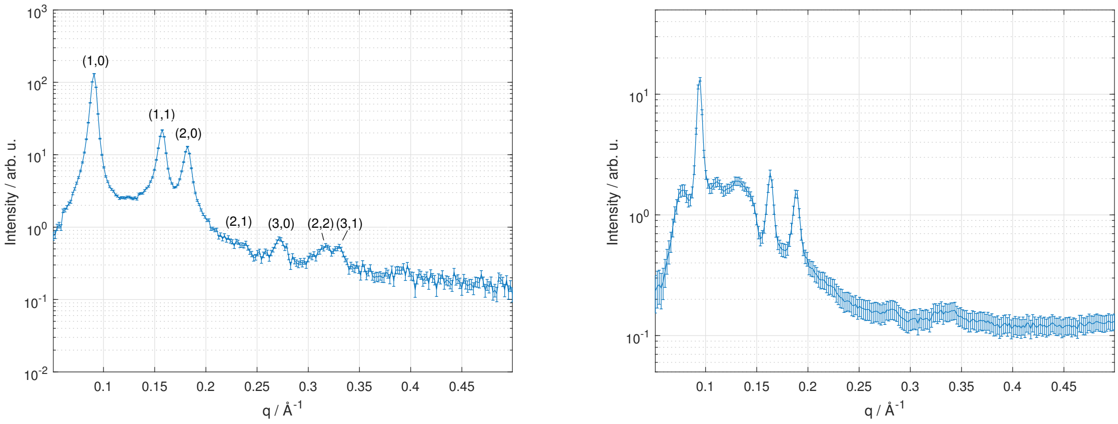

Figure 3.3: SAXS-spectra from pure DOPE samples.
Left side: DOPE + 12% tricosene (35 °C), right side: DOPE + 13% squalene (35 °C)

In spectra of mixed aggregates (figure 3.4) one can observe the same structure of peaks, however, as the concentration of guest lipid rises, their intensity as well as the number of visible peaks decreases. Additionally, if $C_{0,guest} > C_{0,host}$, a higher amount of guest lipid shifts the peak positions to lower q-values, which means that the cylinder diameter increases.

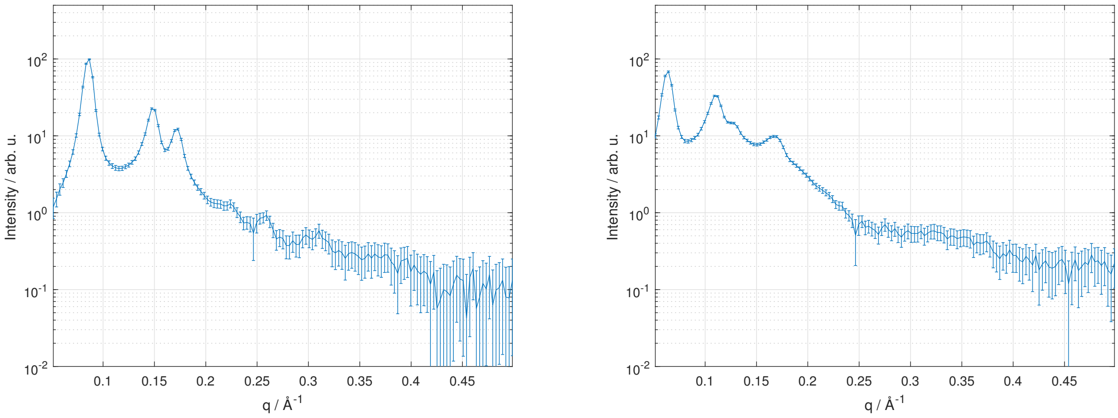

Figure 3.4: SAXS-spectra from mixed samples.
Left side: DOPE + 10 mol% Egg Sphingomyelin (40 °C),
right side: DOPE + 30 mol% Egg Sphingomyelin (40 °C)

3.2 Influence of the filler molecule

A challenging aspect of measuring intrinsic curvatures is that one has to produce stress-free monolayers. In our model system the filler molecule is thought to facilitate this. Therefore it is crucial to understand what happens between the lipid cylinders. As a parameter of how well the filler incorporates into the aggregate, we can use the lattice constant a.

If there is no or not enough filler, lipids have to occupy the space between the cylinders. One part of the lipids stretches into the corners of the hexagon while the others have to bend to the sides or interdigitate with the tail groups of the neighboring cylinders. In both cases these hydrocarbon chains cause a higher mean curvature than the relaxed lipid would have, thus result in smaller cylinders.

If the filler molecules interdigitates with the lipid tail groups, a should also decrease, because if more space is occupied by the hydrocarbon chains, again the curvature rises.

If there is too much filler molecule, it will try to enter the hydrophobic region between the cylinders and push them apart. This can result in packing defects of the lattice, as shown in figure 3.5. These defects might add undesired details to the diffraction spectrum.

An increase of a in respect to the optimal, relaxed case would only be possible if all cylinders are pushed apart by the filler molecule. However, in this case they would easily fluctuate and a regular hexagonal lattice would be unlikely. Thus, we are looking for the configuration with an unperturbed spectrum and the highest possible a.

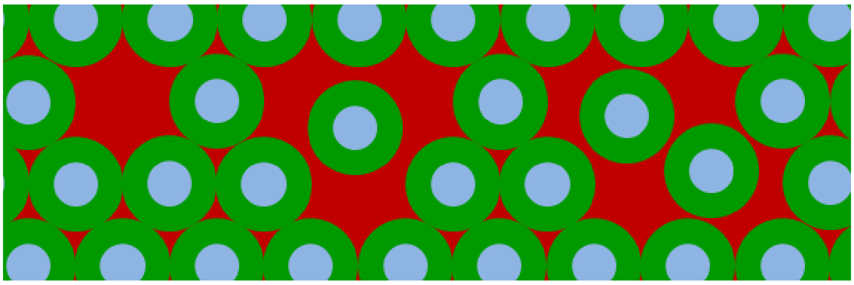

Figure 3.5: Lattice defects in the hexagonal lattice. The order of the lipid (green) cylinders with water cores (blue) is distorted by a too high amount of filler molecules (red).

As indicated in section 1.1.2 we tested squalene as an alternative filler and prepared various samples to explore its influence in different concentrations. It was observed for tricosene ([2],

black line in figure 3.6) that a reaches a plateau around 12 wt% ($\approx$ 12.5 vol%) and at 15 wt% ($\approx$ 15.8 vol%) additional features in the spectrum were observed. For squalene, already at 13 wt% ($\approx$ 13 vol%) deviations appeared.
Lattice parameters are also significantly smaller for squalene than for tricosene samples at the same volume fraction. This indicates that there are interactions in the tail groups in these samples (interdigitation, bending/stretching, other interactions with squalene).
The largest lattice constant was reached with the sample 3a, using 12 wt% tricosene. The different result for sample 3b indicates that the amount of tricosene is not the only factor of influence. Documented differences in preparation are the reduction of the vortex speed from 1800 rpm (3b) to 600 rpm (3a) and different lipid solutions (30 mg/ml for 3b, 10 mg/ml for 3a).

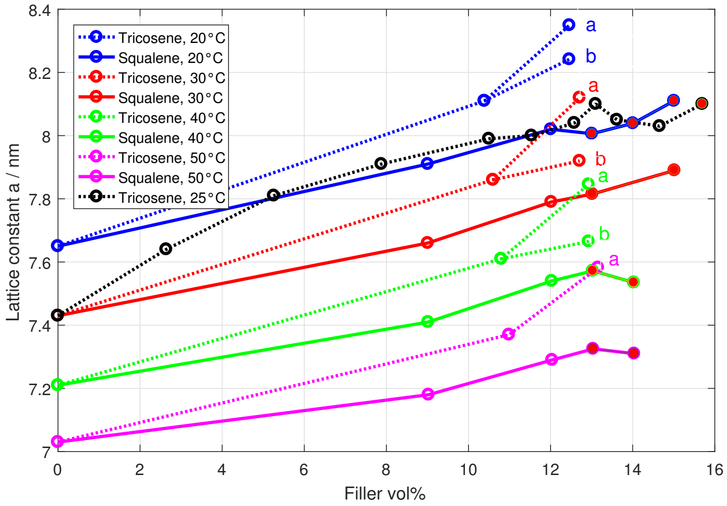

Figure 3.6: Lattice constant a of DOPE H_{II} phases in dependence of filler concentration and temperature. Wt% were converted to vol% for better comparability. Data points with red filled markers did not form pure H_{II}-phases.
Measurements of the aggregates with tricosene at 25 °C are taken from [2].
Measurements marked with a and b refer to samples 3a and 3b.

Inserting these results into (2.2.2) together with our estimated aggregate diameter D from the microscopy images, we acquire a lattice order of around $n = 50$.

3.3 Results from the global scattering data analysis

Our idea about the global analysis, would be to first evaluate data from pure samples to obtain a parameter set for the host lipid and to use these parameters for the analysis together with a guest lipid. The global analysis was tested for some of the prepared samples. The analysed q-range was 0.05 to 0.5 Å^{-1}. Monte Carlo runs were done with 10^5 sweeps, starting once with a guessed parameter set (either from a DE-analysis or with knowledge from previous related problem) and 3 times starting from random positions. Runs that did not converge within the burn-in phase ($2 * 10^4$ sweeps) were excluded from further calculations. For DE-runs we used $F = 0.4$, $CR = 0.7$ and a population size of 10 times the parameter size.

3.3.1 Single lipid

This analysis was mainly done for DOPE. PE-lipids are a well researched molecule group, so there is some prior information that we can use. The following parameters were fixed in the fitting routine:
The backbone width was chosen to be $d_{BB} = 3$ Å. This was done to avoid correlations with other parameters (C_0, d_H) and justified by the rigidity of the backbone structure. The values were estimated from SDP-analysis of lamellar phases. Headgroup and backbone volumes are also expected to coincide with these data ($V_{PE} = 245$ Å^3 and $V_{BB} = 0.55\ V_{PE}$) and were fixed (Source for all data: [30]).
About the total lipid volume of DOPE in the H_{II}-phase there is very little reliable data. In figure 3.7 we see the resulting fits for DOPE with tricosene (sample 3a) and squalene (sample 5). In both cases there is no optimal agreement, but the data of the sample with tricosene ($\chi^2 = 11800$) seems to fit better to the model than the data of the one with squalene ($\chi^2 = 30400$). This agrees with the results from section 3.2, that tricosene is the better choice as a filler. All further results in this section were evaluated from measurements of sample 3a.

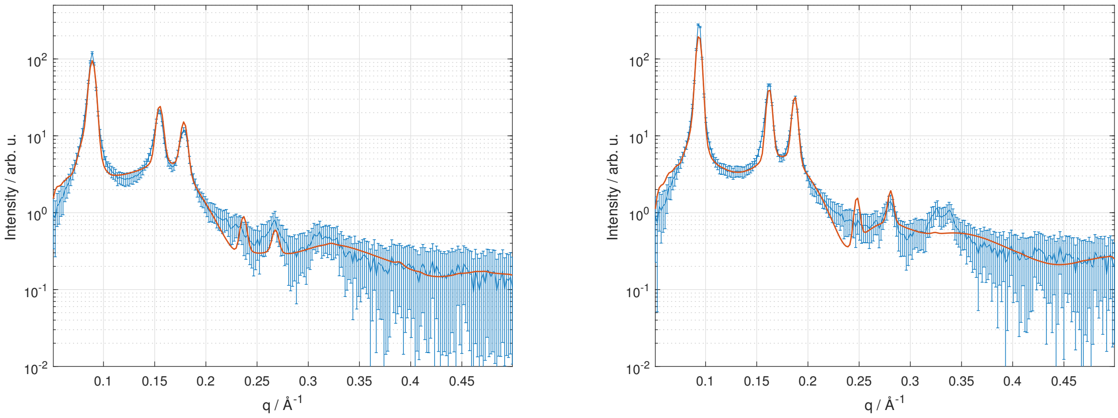

Figure 3.7: X-ray scattering data (blue) and fits (orange) for DOPE-samples.
Left side: DOPE + 12 wt% tricosene, right side: DOPE + 12 wt% squalene. Both samples were measured at 30 °C.

The details of the fitting curve of the tricosene sample can be seen in figure 3.8. One can see that the bilayer form factor compensates for the form factor minimum between the (1,0) and the (1,1)-peak. The (2,1)-peak has almost vanished in the data, which is due to the concurrence of structure factor peak and form factor minimum as seen in the data between 0.2 and 0.25 Å^{-1}. However, the solution where they fully overlap and the peak vanishes is never a good result according to fitting routines. The reason is that the deviation that would occur right after the (2,0)-peak (as can be seen from the form factor just below 0.2 Å^{-1} in the figure) gives a higher

penalty to the χ^2 than the deviation in the shown solution.
The electron density profile used in the form factor (right side of the figure) has an expected shape. A small headgroup width causes a relatively high difference in electron density to the outer parts of the lipid. Unexpected is the difference in electron density between the lipid hydrocarbon chain and tricosene. This is linked to a rather small total lipid volume resulting from the fit, as discussed below.

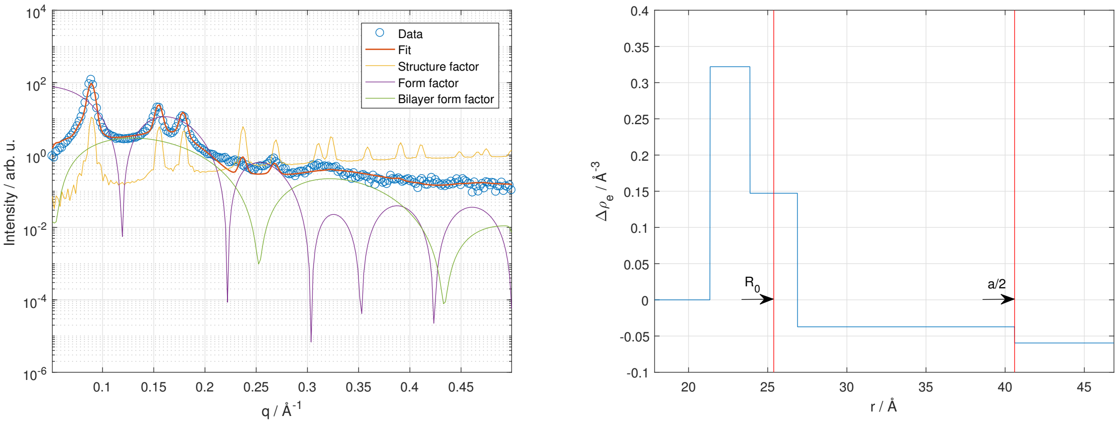

Figure 3.8: Details of the fitting curve shown in figure 3.7, left.
The left graph shows the components that the model uses for the fit. Right side: radial electron density profile of the hexagonal prisms used for the form factor.

MCMC analysis

The following data show the results of 3 converged MCMC runs, for the sample 3a at 30 °C. Looking at marginal posteriors, we see the distribution of likely values as well as correlations between parameters. The most significant correlation of parameters is that of C_0 and d_H (figure 3.9). The 2D-plot shows a valley of likely solutions along a straight line of equal inner radius of the lipid cylinder. The radius of the oil-water interface also contributes, since the likelihood increases at lower C_0- (and d_H-) values. The abrupt drop at small d_H is due to a break criterion in the algorithm, which is triggered when the headgroup volume exceeds the volume of the slab which should accommodate it (and therefore negative H_2O molecules would be necessary.).
Choosing a value as well as estimating the uncertainty of C_0 is difficult because of the non-symmetric distribution. As we need a parameter set of DOPE (C_0, d_H, d_{BB} and V_{lipid}) for fitting the lipid mixtures, one choice would be the set with the lowest χ^2, that was found in the run (marked red in the figures).
Another possibility would be to choose a d_H (or C_0) and to use a horizontal (vertical) slice from the 2D-distribution and calculate mean and variance from the resulting, roughly Gaussian, distribution for C_0 (An example is shown in figure 3.9, right. Its quality could be further improved by a higher number of samples). d_{BB} was chosen in advance and V_{lipid} is uncorrelated, thus we could take its mean value. For further results, the most likely set was chosen.

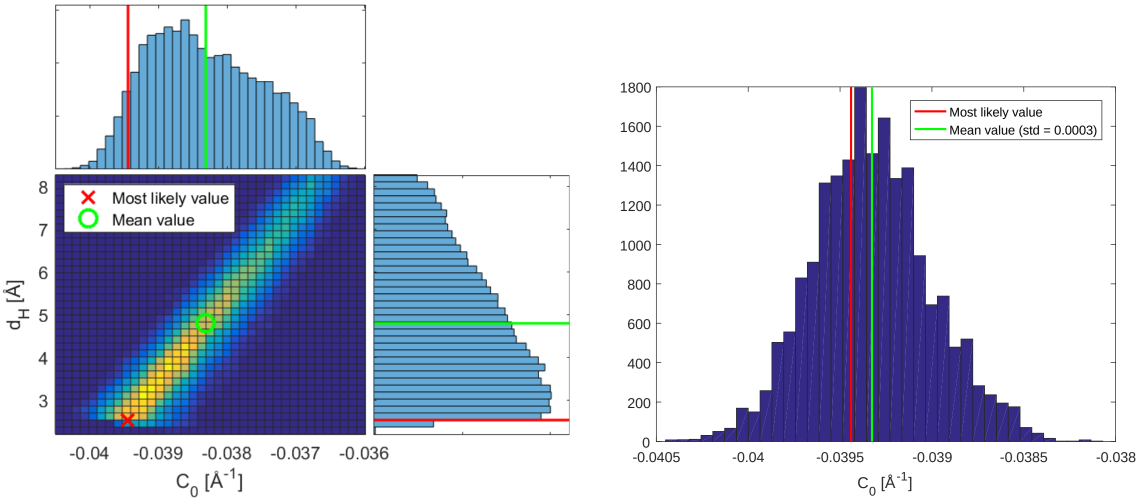

Figure 3.9: Left side: Marginal posteriors of intrinsic curvature C_0 and headgroup width d_H. Bright colors in the 2D-plot depict high number sof samples.
Right side: Distribution of samples with $d_H \leq 2.8$.

The samples was measured for various temperatures, the results display a linear behaviour (see figure 3.10). Compared to measurements using the former method ([31]), the slope is slightly different, the errors are in the same order of magnitude. In the temperature range from 20 to 50 °C the results coincide within their error ranges.

$$Intrinsic\ curvature\ of\ DOPE:\ C_0 = -0.334 - 0.0019 * T \pm 0.01\,\mathrm{nm}^{-1}$$

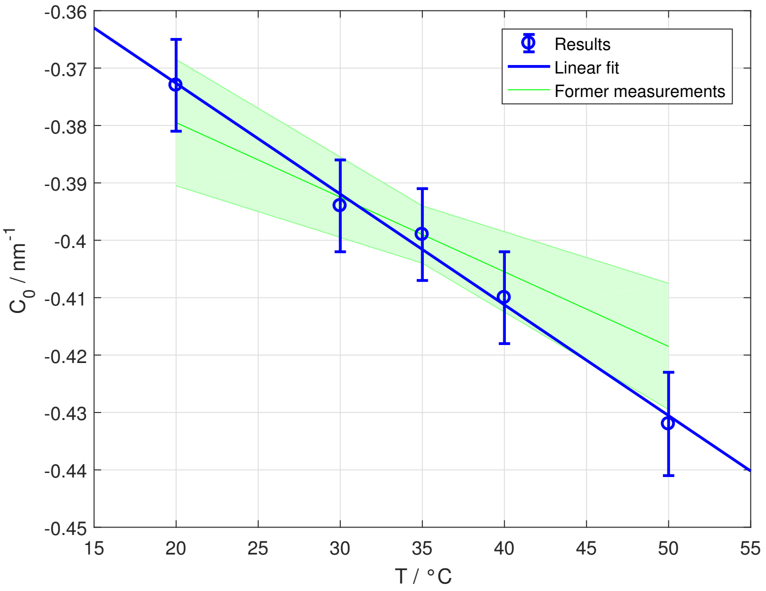

Figure 3.10: Intrinsic curvature of DOPE. Former measurements taken from Kollmitzer et al. [31]

A parameter that was rather well determined is the total lipid volume (which effectively determines the tail group volume, since the volume of the headgroup is fixed). In the model it has no influence on the cylinder structure, but defines the electron density of the hydrocarbon chains. One can see in figure 3.11, left, that the correlation between V_{lipid} and C_0 is negligible and that the samples are approximately normal distributed in V_{lipid}. Measured for various temperatures,

V_{lipid} results to be constant 1160 ± 25 Å^3. The constant behaviour was also observed in [32], however the value there is about 15 % higher.

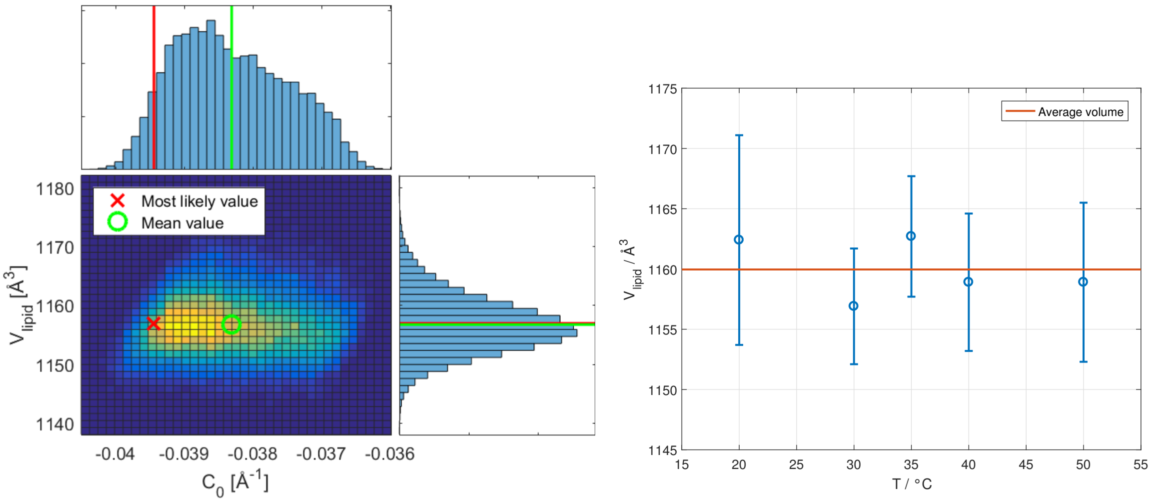

Figure 3.11: Volume V_{lipid} of DOPE in the H$_{II}$-phase.
The left subfigure shows marginal posteriors of V_{lipid} and C_0 as well as their correlation. On the right the results for measurements at different temperatures are shown.

Probability distributions according to MCMC for the remaining parameters are shown in figure 3.12. We see that most of them are well defined and their distributions show Gaussian shapes. The exception is the correlation between area per lipid and number of water molecules in the lamellar phase. These show a similar correlation as C_0 and d_H. In this case, the bilayer thickness is determined through both parameters and is here the decisive parameter for the shape of the bilayer form factor.

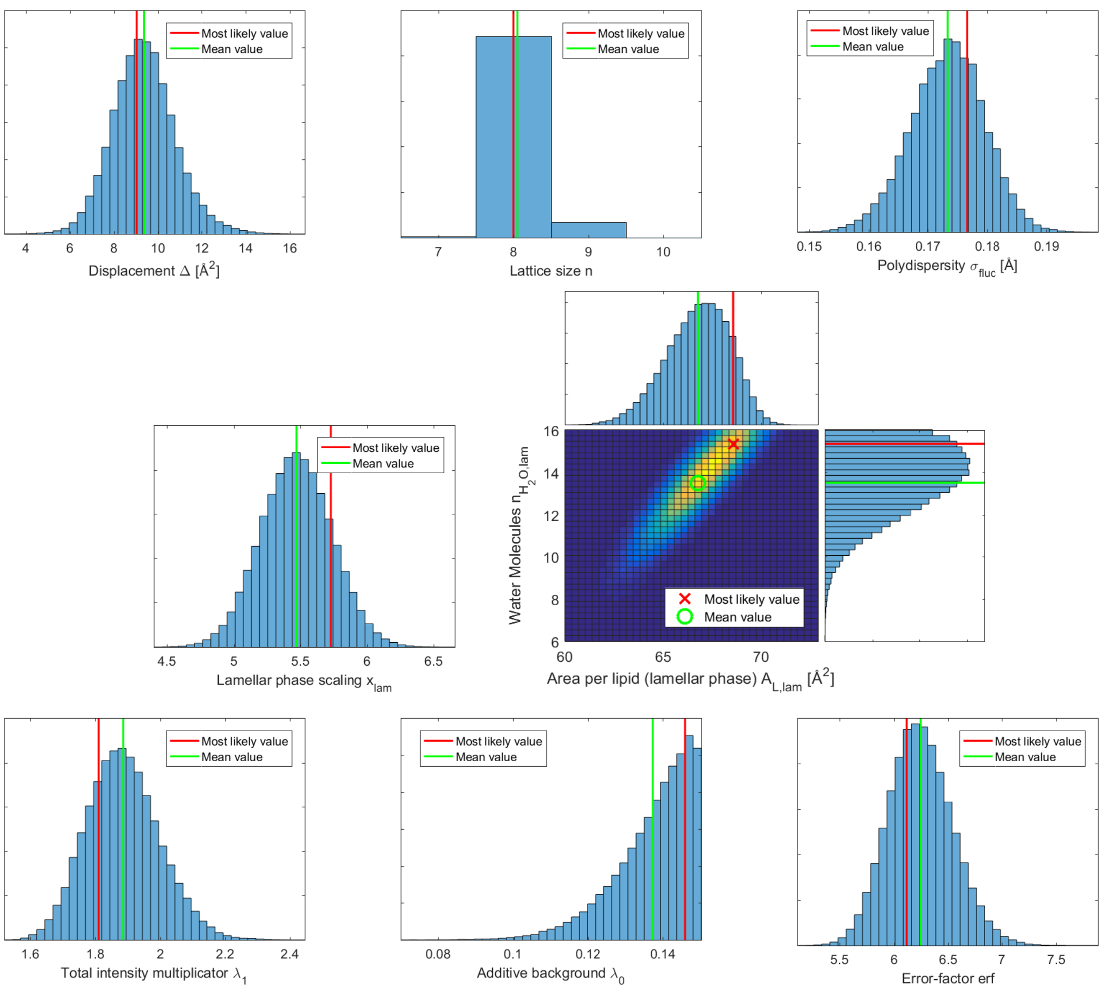

Figure 3.12: Marginal posteriors of all other varied parameters. Correlations and deviations from a gaussian shape are only observed for headgroup area and the number of water molecules (both parameters of the bilayer form factor).

To estimate the quality of the MCMC analysis, we look at the timeline of the parameters (figure 3.13). Parameters with long autocorrelation times τ are d_H and C_0, as expected from their correlation (they are only able to move together). Also the lattice size has long autocorrelations, which might be due to the rather large change induced by a step in lattice order. However, runs from different starting points result in the same value, which is a good indicator for the quality of the value. To make up for the autocorrelations, computation time (number of iterations) was adjusted, so that they are small in comparison to the total time. All other parameters have smaller values τ and show a noise-like behaviour in the time plot, as desired.

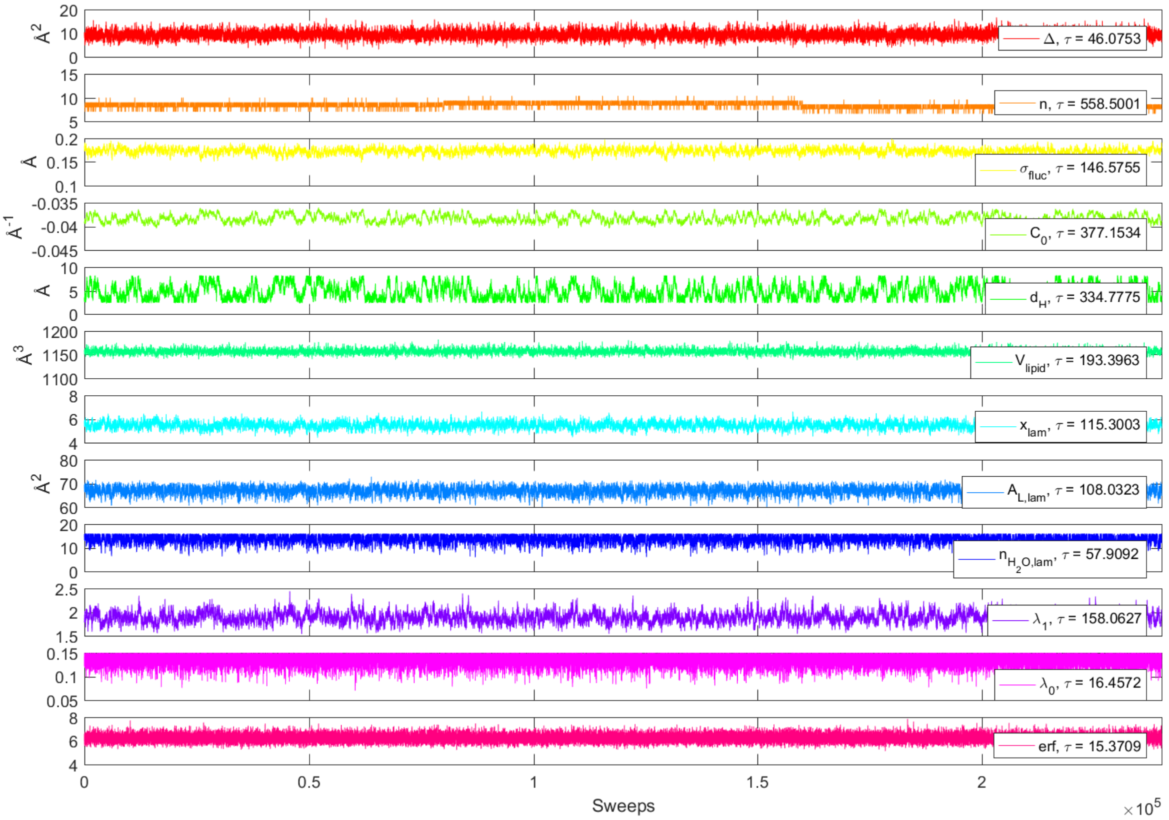

Figure 3.13: Timeline of all varied parameters in the MCMC-run with DOPE at 30 °C.

Further analysis of the temperature series

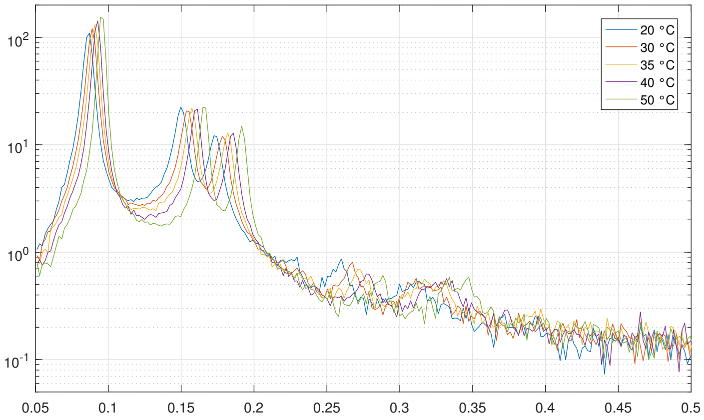

Figure 3.14: SAXS-temperature series for sample 3a (DOPE + 12 wt% tricosene)

In table 3.1 we see the resulting parameter sets for DOPE from MCMC analysis of the spectra shown in figure 3.14. Parameters show either a constant or a monotonous behaviour in temperature.

Interestingly the disorder parameter Δ does not increase with temperature as one would expect. Also the increase in lattice size n does not seem intuitive, since steric repulsions between the cylinders might increase.

The unit cell fluctuations also do not seem to increase with temperature, which might be a hint that this parameter σ_{fluc} is more a measure for cylinder deformation, lipid buckling/stretching and rotation than for actual movement of the molecules.

The interfacial area per lipid A_{if} is rising with temperature, as expected, but the behaviour does not seem to be linear.

x_{lam} is a measure for the amount of lamellar phase in the sample, however its absolute value has no physical meaning. The necessity of a lower amount at high temperatures can seen in figure 3.14: Although the height of the first peak increases, the minimum intensity between the peaks decreases.

Further, because we see a correlation between $A_{L,lam}$ and $n_{H_2O,lam}$ there is no certainty that their values have a physical meaning. Since they are responsible for the shape of the bilayer form factor together, one could try to combine them to a single parameter.

λ_0 and λ_1 are scaling parameters without physical meaning. It is reasonable that they are consistent for a single measurement series.

The value of erf suggests that the actual errors of the measurement are 5 to 7.5 times higher than expected. This is an indicator for the disagreement between model and reality.

Table 3.1: Most likely parameter sets for DOPE. Bold quantities are to be used in the analysis of mixed samples.
* not a fit parameter, but evaluated from the others.

T [°C]	20	30	35	40	50	Error
Δ [Å^2]	8.47	9.03	10.18	9.94	7.88	2
n	7	8	10	13	18	1
σ_{fluc} [Å]	0.174	0.177	0.173	0.173	0.173	0.007
$\mathbf{A_{if}}$ * [Å^2]	53.0	52.8	54.4	59.1	63.4	
$\mathbf{C_0}$ [Å^{-1}]	-0.0379	-0.0394	-0.0400	-0.0410	-0.0432	0.001
$\mathbf{d_H}$ [Å]	2.47	2.53	2.97	3.18	4.81	0.7
$\mathbf{V_{lipid}}$ [Å^3]	1164	1157	1161	1159	1156	25
x_{lam}	6.2	5.7	5.2	4.9	4.4	0.5
$A_{L,lam}$	70.4	68.6	66.0	65.6	65.1	2
$n_{H_2O,lam}$	17.7	15.4	11.8	10.2	8.9	2.2
λ_1	1.72	1.81	1.81	1.82	1.90	0.2
λ_0	0.149	0.146	0.150	0.141	0.148	0.02
η	6.1	6.2	5.3	5.4	6.2	0.3

Analysis by differential evolution

In contrast to the Monte Carlo sampling we tested a pure fitting routine. Its advantages are expected to be a much faster evaluation and possibly a better convergence to the global minimum. The results for DOPE at 30 °C shown in table 3.2 were acquired in 90 min (using 500 iterations per fit), in contrast to a duration of 11.5 h for the MCMC-analysis. Also, parameter with better fit quality have been found ($\chi^2 = 11430$, fig. 3.15 right, versus 11700 for MCMC), however with slightly different curvature values ($C_0 =$ -0.0385 versus -0.0395). The fits do not seem to converge to the lower boundary of d_H as the MCMC analysis suggests, but are closer to the mean value of the distribution (figure 3.9, left).

Table 3.2: Results from 10 DE-runs for DOPE at 30 °C with with 500 iterations each.

Fit No.	C_0 [Å^{-1}]	χ^2
01	-0.0382	11630
02	-0.0385	11430
03	-0.0378	11480
04	-0.0388	11580
05	-0.0388	12060
06	-0.0384	11520
07	-0.0390	11540
08	-0.0389	11680
09	-0.0382	11580
10	-0.0382	11520

The method seems to converge to its final C_0-value already within about 150 iterations (figure 3.15, left), with no further change afterwards. This suggests, that the method might have trouble dealing with the correlation between C_0 and d_H and gets stuck easily at some point with in the correlation valley.

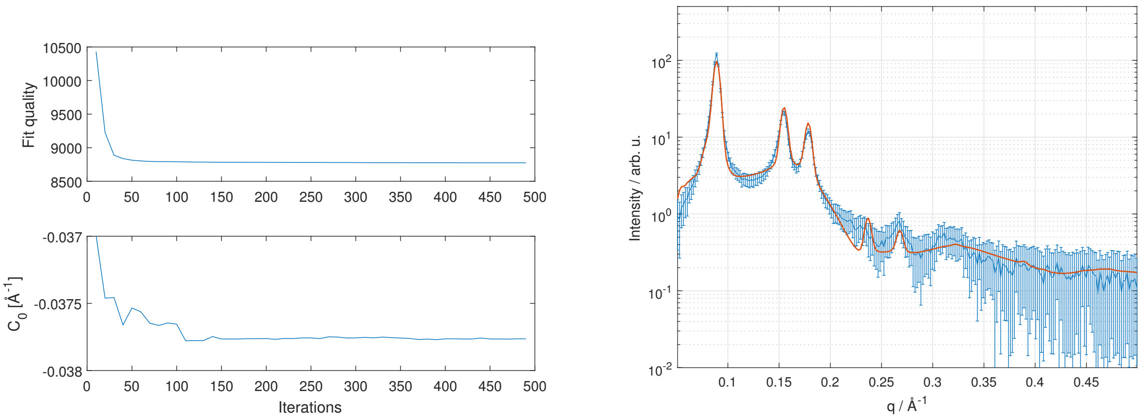

Figure 3.15: Differential evolution fitting results for DOPE at 30 °C.
The left figure shows how the fit quality (algorithm intern unit) and C_0 converge.
The right figure shows the best acquired fit (No. 02 from table 3.2).

For other temperatures the results show a similar distribution, which makes the result less consistent and linear. The temperature profile is shown in figure 3.16. The alternative result, acquired by differential evolution is:

$$\textit{Intrinsic curvature of DOPE}: \; C_0 = -0.329 - 0.0017 * T \pm 0.01\,\mathrm{nm}^{-1}$$

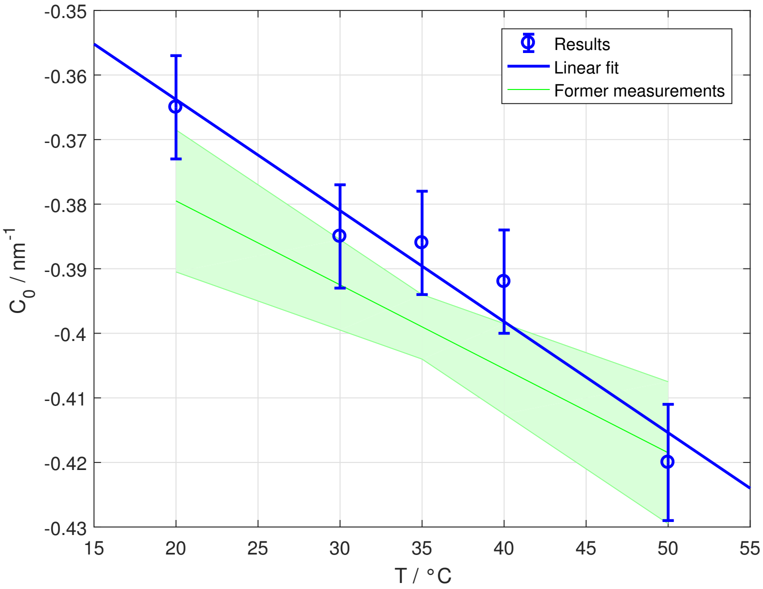

Figure 3.16: Intrinsic curvature of DOPE, acquired by DE. Former measurements taken from Kollmitzer et al. [31]

DMPE

There was also one suitable spectrum obtained by using DMPE in pure form at 80 °C. The spectrum looks slightly different, since also the (2,1)-peak is visible. It was analysed by DE, the best fit is shown in figure . It is of lower quality than for DOPE, but the consistency of the DE-runs is very high (table 3.3).

$$Intrinsic\ curvature\ of\ DMPE\ at\ 80\,°\mathrm{C}:\ C_0 = -0.285 \pm 0.01 nm^{-1}$$

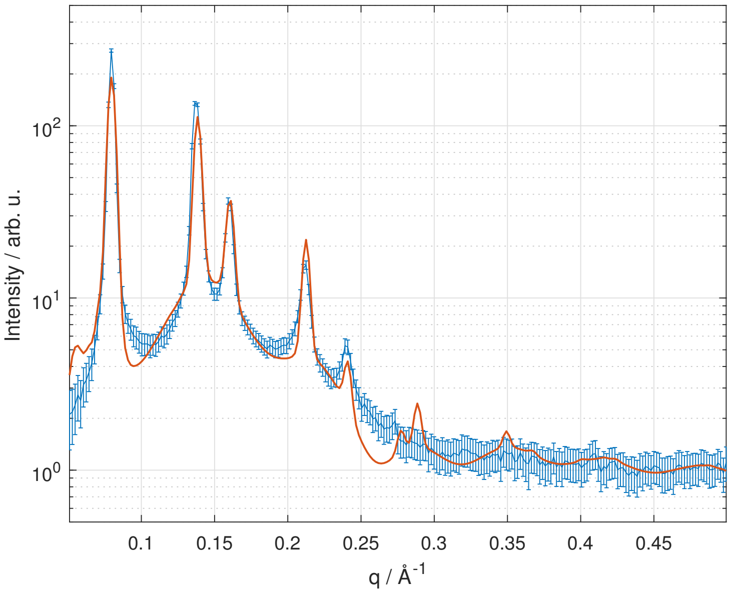

Figure 3.17: SAXS-measurement of DMPE at 80 °C including best fit acquired by DE

Table 3.3: Results from 10 DE-runs with with 200 iterations each.

Fit No.	C_0 [Å^{-1}]	χ^2
01	-0.0285	53950
02	-0.0285	52890
03	-0.0285	53380
04	-0.0285	55260
05	-0.0285	54940
06	-0.0285	452930
07	-0.0286	54510
08	-0.0285	55200
09	-0.0285	56210
10	-0.0285	55470

3.3.2 Lipid mixtures

In the evaluation of SAXS-spectra from mixed samples we used the parameters for DOPE given in table 3.1. Fixing these parameters is beneficial for the data evaluation, since the number of parameters is the same as for the single lipid. However, using MCMC the acquired errors will possibly be smaller than the ones given in the results, since these parameters are not allowed to vary. Again, The backbone volume was fixed to 3 Å, the PC-head and backbone sizes size set to $V_H = 331$ Å^3 and $V_{BB} = 0.42V_H$[33]. For sphingomyelin: $V_H = 331$ Å^3 and $V_{BB} = 0.42V_H$ (from private communication with Fred Heberle). Lipid volumes were taken from [14].
The presented results have been acquired by MCMC. Fitting curves at low guest lipid percentages x (figure 3.18 a) are of similar quality as for pure samples. For higher concentrations (figure 3.18 b,c) it deviates more, especially a form factor minimum right after the (3,0)-peak becomes more and more pronounced in the model.

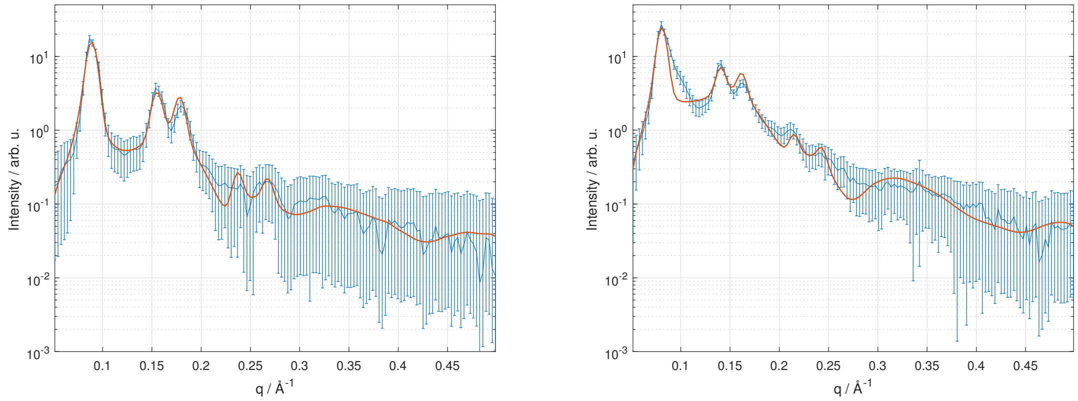

(a) 10 mol% DPPC (b) 20 mol% DPPC

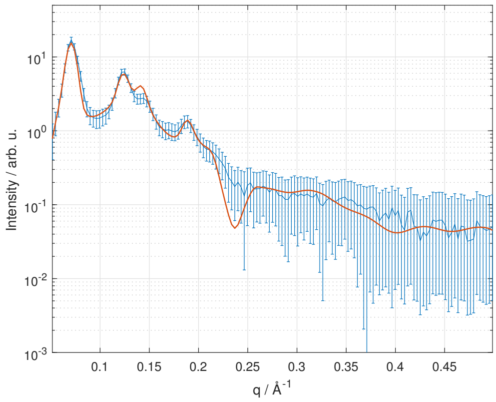

(c) 30 mol% DPPC

Figure 3.18: Fits for samples of DOPE with DPPC at 50 °C

The headgroup width-curvature correlation seems to be less relevant for lipid mixtures (see figure 3.19). For low concentrations of guest lipid, the headgroup size is expected to have only minor influence, since the electron density of the guest lipid is weighed by x. For lipids with PC-headgroups, d_H tends to its upper limit. This might be due to their bulkiness compared to the PE-headgroup. Also the angular headgroup size b_{guest} is larger than that of DOPE, however a physical consistent value was only found for 10 and 30 mol% guest lipid concentration..

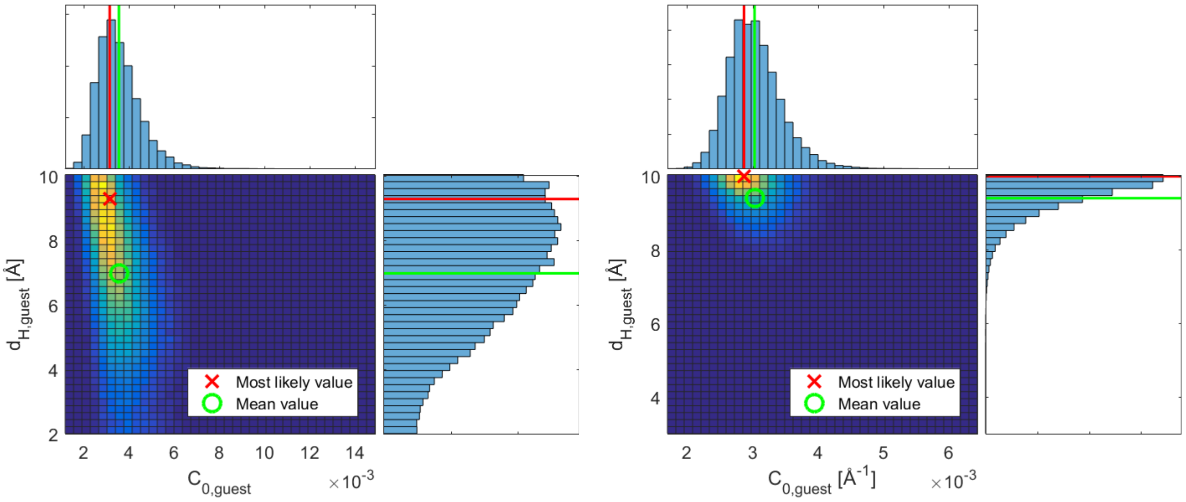

Figure 3.19: C_0-d_H correlations for DOPE + 10 mol% DPPC at 50 °C (left) and DOPE + 10 mol% SM (right)

Table 3.4: Most likely parameter sets for DPPC at 50 °C.
* determined from peak positions. ** calculated by (2.17)

x_{DPPC}	10 mol%	20 mol%	30 mol%	Error
a * [Å]	81.2	89.5	101.9	
Δ [Å^2]	9.6	18.7	28.9	5
n	5	6	4	2
σ_{fluc} [Å]	0.129	0.106	0.121	0.009
b_{guest}/b_{DOPE} **	1.37	1.11	1.37	
C_0 [Å^{-1}]	0.0031	0.0034	0.0011	0.003
d_H [Å]	8.271	4.593	9.89	2.1
x_{lam}	4.15	8.5	7.61	0.6
$A_{L,lam}$	63.4	68.8	65.4	2.6
$n_{H_2O,lam}$	6.7	15.9	16.0	2.7
λ_1	0.52	0.62	0.42	0.09
λ_0	0.029	0.040	0.040	0.009
η	2.6	2.2	1.6	0.2

The results suggest that there is around twice as much lamellar phase at concentrations 20 and 30 than for 10 mol% DPPC (similar for SM, see Appendix tab. i). If this is the case, there might be an inclination of the guest lipid to join the lamellar phase, which would cause a reduced molar fraction in the H_{II}-aggregate. We want to do a rough estimation for the error caused by this effect. Assuming independent (no off-diagonal terms in the covariance matrix), Gaussian distributed variables, we can estimate the influence of a smaller amount of guest lipid in the hexagonal phase:

$$\Delta C_{0,guest}(\Delta x) = \left| \frac{\partial C_{0,guest}}{\partial x} \right| \Delta x, \tag{3.1}$$

whereby we derive from (2.15):

$$C_{0,guest}(x) = \frac{1}{x} \frac{C_0 - C_{0,host}}{b_{guest}/b_{host}} + const. \tag{3.2}$$

For $C_{0,guest} > C_{0,host}$, $C_0 - C_{0,host}$ is always positive. Thus decreasing x increases $C_{0,guest}$. Evaluated for the 10 mol% DPPC sample (50 °C) and assuming that x could be 2 mol% lower than intended, we get an additional error for the measurement:

$$\textit{Error caused by lower guest lipid concentrations} : \Delta C_{0,guest}(\Delta x = {}^{+0}_{-2}\ \text{mol\%}) = {}^{+0.009}_{-0}\ \text{Å}^{-1}$$

As mentioned above, also the errors resulting from the single lipid analysis have not been included. They might also be introduced in the same way.

Figure 3.20 shows results for different guest lipid curvatures. Errorbars denote the pure standard deviations resulting from MCMC (no inclusion of the errors mentioned just above). One can see that the results agree rather well for different amounts of DPPC and SM, but for DLPE and DMPC the difference is rather large. The common parameter of these characteristics seems to be the tailgroup length. The hydrocarbon chain length of DPPC and SM (16:0) closely matches that of DOPE (18:1, the double bond is assumed to shorten the chain), while that of DMPC (14:0) and DLPE (12:0) do not. Hence, the chainlength mismatch between short chain lipids and DOPE seems to impede the analysis in terms of the currently applied model.

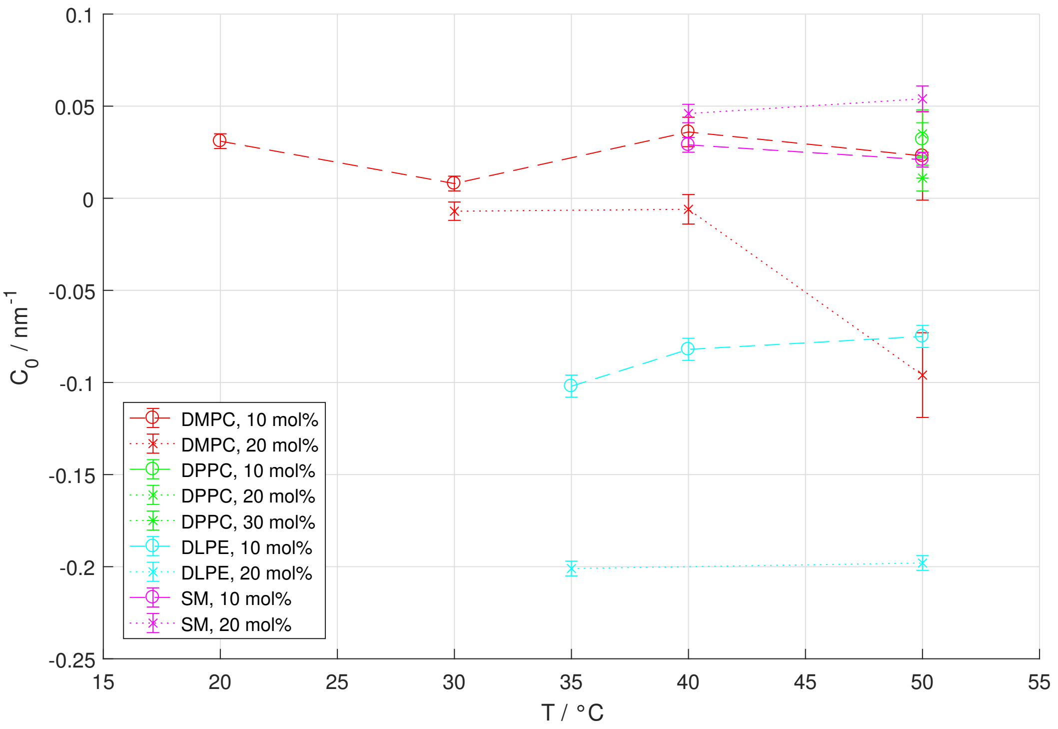

Figure 3.20: Resulting curvatures for different guest lipids acquired by MCMC.

In the case of DPPC we can observe the effect of the curvature addition using headgroup sizes (2.15). Figure 3.21 shows the total curvature in dependence of the lipid ratio x calculated for the analysed DPPC-samples, as well as the linear extrapolation done in [2]. One can see that the results for the total curvature from this analysis agree with the former ones, but using equation (2.15) they result in different values for $C_{0,DPPC}$.

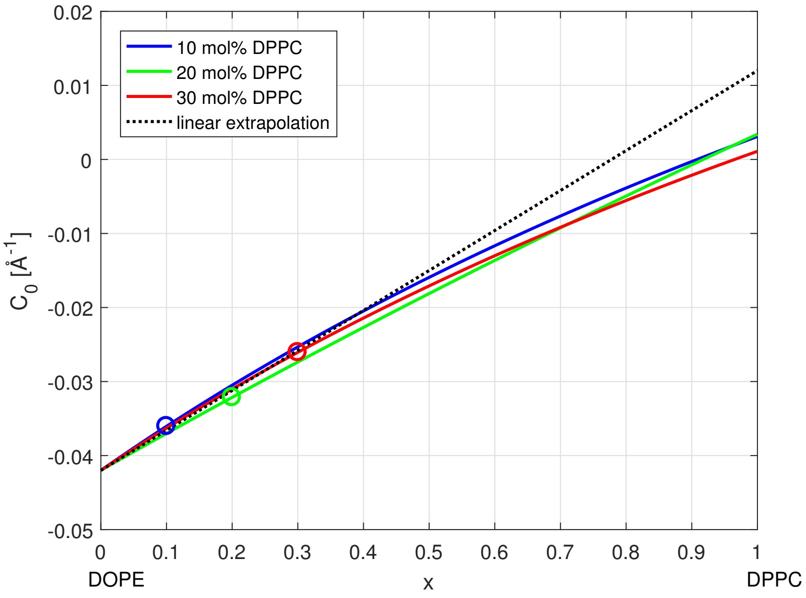

Figure 3.21: Total monolayer curvature depending lipid composition in a DOPE-DPPC mixture.

4 Discussion

Looking at the whole method *global X-ray scattering data analysis of inverted hexagonal phases* we have to discuss several levels of complexity. Since the sample is created solely for this measurement, there are two parameter-systems to adjust: the model system and the model. In addition, there are different ways to analyse the data given by the X-ray scattering, which is the only part of the analysis which is fixed from the beginning.

The procedure of sample preparation (RSE) was originally invented for liposomes [21], but works fairly well to produce $\mathrm{H_{II}}$-aggregates. The result seems to be very robust to several parameters (temperature, solution, vortex speed, etc.). However, reproducibility of the aggregate dimensions needs to be checked rigorously.

A decisive parameter that was already analysed rather well is the amount of filler molecule.[34, 13, 35, 12] Aggregates grow with increasing amount of filler until deviations from a pure hexagonal phase occur.[2] However, the reproducibility of the lattice parameter (which is equal to the cylinder size) is not yet fully examined. Sample 3a is significantly larger than the others, which would in theory suggest it to be the best sample, however the reason for being larger and thus the reason for the other samples to be smaller has to be investigated. If the optimal lattice parameter for every temperature of DOPE is known, it can be a very good indicator for successful preparations. For lipid mixtures, the exact relation between guest/host lipid ratio and lattice parameter would also be interesting to examine.

Another crucial point in the preparation concerns the mixing of host and guest lipid. In general, we do not know how much of the guest lipids incorporates into the hexagonal aggregate and if there is an enrichment of guest lipid in the coexisting lamellar phase. Furthermore, there might be an effect of demixing or domain formation at temperatures below the guest lipid's melting point, as the failed MCMC-runs for these measurements suggest. This effect might be reduced by heating the sample above the guest lipid melting temperature before measuring at the desired temperature.

The time between preparation and measurement apparently has no impact on the measurement. It has shown that keeping mixed aggregates 1-2 days at room temperature or higher (but below 70 °C, where double bonds start to oxidise) helps them reach their equilibrium state.

On the other hand there is the task to create a model that represents the actual structure of the sample well enough. However, adding more details increases computation time and involves the danger to over-determine the system or might be simply wrong and lead to wrong conclusions. The vaguest part of the model is probably the bilayer form factor, which is mainly justified by the shape of the observed spectrum (absence of a minimum between the first 2 peaks). A result that supports this assumption is the increase of the lamellar scaling factor with higher amounts of DPPC in the sample. Also for the SM- and DMPC-samples the value is higher for 20 mol% guest lipid than for 10 (see tables i,ii). It would be advisable to investigate if this is a recurring feature.

The slab model for the electron density obviously assumes a simplicity not given by nature. However, the difference in the form factor comparing to the more complex SDP-model (see [33]) has turned out to be negligible. This might be caused by the inclusion of fluctuations, which do not distinguish between rotations, movement and buckling/stretching of the lipid and also cause an overlap between the molecular groups, as also the SDP-model does.

A problem that arises in the mixed aggregates is the location of the tail groups. If the hydrocarbon chains of host and guest lipids have different lengths, the longer chains could bend over the shorter ones and change the shape of their unit cell. This could be a general drawback in the utilization of curvature as a parameter describing heterogeneous membranes, which impedes the additivity of curvature. For this method it means that for lipids of different tail groups we would either need a theory about the interactions of hydrocarbon chains of different length or a set of host lipids to always match the chain length of the guest.

The X-ray scattering was not attempted to be optimized. One detail should be mentioned: Some measurements show higher resolution, which means that the shape of the high-q peaks is better defined. However, these peaks are still not reproducible by the model, thus a higher resolution is not necessary. One could even think of shortening measuring times.

The next step is comparing model and data and to answer the question: How can we be sure that what we observe is what we believe it is? Optimal fit quality is not given and some parameters are connected in complex relations.

MCMC gives an overview of the situation. Insights about correlations and probabilities have given good impulses for the work. However, since the MC-chain moves through parameter space slowly, the calculation is rather expensive and the chances that an optimal parameter set is not found are still high. Furthermore, the analysis of mixed lipids was fed from the single lipid analysis by parameter values without any variance. However, some of these parameters have complex probability distributions, which should be respected in the calculations. Doing this efficiently would require to code the analysis in a lower level language than Matlab.

Differential evolution (or fit algorithms in general) might be a better approach for a quick and efficient curvature measurement. However, this algorithm seems to be fragile to certain kinds of correlations. Corrective actions could be either to optimize mutation rate and crossover for the data, to use a number of consecutive fits or to try even another method (simulated annealing, etc.).

Regarding the results, we see that for the single lipid analysis there are still problems to reliably resolve the headgroup. MCMC sampling distributions for DOPE have their maximums at low d_H, but the mean values are rather far away from this solution. The linear correlation to C_0 causes a rather wide distribution of results in both MCMC and DE. It has been shown that if one could narrow the possible d_H, one could reduce the error by a factor of 3 (figure 3.9). Here, data from molecular dynamics simulations could give insight.

Small d_H-values, which correspond to headgroups tilted towards the monolayer, have been observed for PE-lipids in lamellar phases and is caused by the attraction of the polar parts of the headgroup. Upon the addition of ions, they have been shown to stretch towards the water ([36]). Adding ions could give insight if this tendency is also given in the hexagonal phase.

As for the result of the lipid volume, the reason for the difference to the literature value is unclear. The fact that the electron density (figure 3.8) of the hydrocarbon chain is different from tricosene gives rise to doubts about the result (the difference would be smaller for a higher value V_{lipid}). A proper density-measurement of tricosene would however be advisable for a better comparability.

As discussed above, the model does not include interactions of tailgroups of different lengths. The short chained guest lipids DLPE and DMPC show a large difference of curvature for different concentrations, which is assumed to be a consequence of the disagreement with the model. For DMPC (14:0) one could test a 16:1-PE host lipid, for DLPE (12:0) an even shorter one would be necessary.

However, also for SM (16:0) there is no perfect agreement for 10 and 20 mol%. There might be still a concentration dependence in the packing of bi-disperse elements. An analysis of more samples of different concentrations could give insight here.

5 Conclusion and Outlook

The task of creating a new technique to evaluate X-ray scattering data of lipid H_{II}-phases was performed and for the most part successful in measuring intrinsic lipid curvatures. The method was able to reproduce literature values for DOPE with potentially higher precision. For lipid mixtures the method seems to be restricted to lipids of coinciding chain lengths. Problems were also found in the miscibility of lipids below their melting temperature, as well as in the determination of the exact amount of guest lipid in the H_{II}-phase. There is also room for improvement in the fitting algorithm, since the currently used techniques can not describe the full complexity of the system efficiently.

Upcoming tasks in the experimental section will be the testing of the reproducibility of lattice parameters and the introduction of a standardized preparation protocol (including the optimal host/guest lipid ratio) and testing of new host lipids of different chain lengths. The model could possibly be improved by introducing considerations about packing, which might explain different results for different guest/host lipid ratios. The data evaluation would profit from being coded in a low-level language, which would enable sampling a higher number of parameters simultaneously. Literature research could be done about molecular dynamics simulations to compare measured parameters. And if for some reason there is still need for higher resolution of the technique, one could think about extending it to a joint-analysis with small-angle neutron scattering (SANS).

Bibliography

[1] B. Kollmitzer et al. “Monolayer spontaneous curvature of raft-forming membrane lipids”. In: *Soft Matter* 9.45 (2013), pp. 10877–10884. DOI: 10.1039/c3sm51829a. URL: 24672578.

[2] Negahbani Neda. *Optimization of inverted hexagonal lipid phase preparation by rapid solvent exchange*. Master’s thesis. Graz, 2016.

[3] *Phospholipid*. http://static.cosmiq.de/data/de/03a/f6/03af633367465f039a831cd63ff09e55_1_orig.jpg. [online, accessed Oct 31, 2017].

[4] Ole G. Mouritsen. *Life - as a matter of fat: The emerging science of lipidomics*. Berlin: Springer, 2005. ISBN: 3-642-42135-8.

[5] Mariana Ruiz Villarreal (LadyofHats). *Phospholipids aqueous solution structures*. https://commons.wikimedia.org/w/index.php?curid=3032610. [online, accessed Oct 31, 2017].

[6] G. W. Feigenson. “Phase diagrams and lipid domains in multicomponent lipid bilayer mixtures”. In: *Biochim Biophys Acta* 1788.1 (2009), pp. 47–52. ISSN: 0006-3002.

[7] G. van Meer, D. R. Voelker, and G. W. Feigenson. “Membrane lipids: where they are and how they behave”. In: *Nat Rev Mol Cell Biol* 9.2 (2008), pp. 112–124.

[8] D. Marsh. “Elastic curvature constants of lipid monolayers and bilayers”. In: *Chem Phys Lipids* 144.2 (2006), pp. 146–159. ISSN: 0009-3084.

[9] N. Dan and S. A. Safran. “Effect of lipid characteristics on the structure of transmembrane proteins”. In: *Biophys J* 75.3 (1998), pp. 1410–1414. ISSN: 0006-3495.

[10] Moritz Frewein et al. “Lateral pressure-mediated protein partitioning into liquid-ordered/liquid-disordered domains”. In: *Soft matter* 12.13 (2016), pp. 3189–3195.

[11] M. M. Kozlov and M. Winterhalter. “Elastic-Moduli and Neutral Surface for Strongly Curved Monolayers - Analysis of Experimental Results”. In: *Journal de Physique Ii* 1.9 (1991), pp. 1085–1100. URL: ISI:A1991GC95400007.

[12] H. P. Vacklin et al. “The bending elasticity of 1-monoolein upon relief of packing stress”. In: *Langmuir* 16.10 (2000), pp. 4741–4748. URL: ISI:000087006200050.

[13] K. Lohner et al. “Squalene promotes the formation of non-bilayer structures in phospholipid model membranes”. In: *Biochim Biophys Acta* 1152.1 (1993), pp. 69–77. ISSN: 0006-3002.

[14] Derek Marsh. *Handbook of Lipid Bilayers, Second Edition*. 2nd ed. Boca Raton, FL: CRC Press, 2013.

[15] Avanti Lipids. *Structure, Product description*. https://avantilipids.com. [online, accessed Oct 31, 2017].

[16] *(Z)-9-Tricosene Fact sheet*. EPA-738-F-94-025. United States Environmental Protection Agency. Sept. 1994.

[17] Ed (Edgar181). *(Z)-9-tricosene biosynthesis*. https://commons.wikimedia.org/wiki/File:(Z)-9-tricosene_biosynthesis.svg. [online, accessed Oct 31, 2017].

[18] André Guinier. *X-ray diffraction in crystals, imperfect crystals, and amorphous bodies*. Courier Corporation, 1994. ISBN: 0486680118.

[19] O. Glatter and O. Kratky, eds. *Small Angle X-ray Scattering*. London, UK: Academic Press, 1982. ISBN: 0-12-286280-5.

[20] N. Freiberger and O. Glatter. “Small-angle scattering from hexagonal liquid crystals”. In: *The journal of physical chemistry. B* 110.30 (2006), pp. 14719–14727. ISSN: 1520-5207. DOI: 10.1021/jp0559332. URL: 16869579.

[21] J. T. Buboltz and G. W. Feigenson. “A novel strategy for the preparation of liposomes: rapid solvent exchange”. In: *Biochim Biophys Acta* 1417.2 (1999), pp. 232–245. ISSN: 0006-3002.

[22] AA Rieder et al. “Optimizing rapid solvent exchange preparation of multilamellar vesicles”. In: *Chemistry and physics of lipids* 186 (2015), pp. 39–44.

[23] O. Glatter. “A New Method for the Evaluation of Small-Angle Scattering Data”. In: *Journal of Applied Crystallography* 10 (1977), pp. 415–421.

[24] S. Förster et al. “Scattering curves of ordered mesoscopic materials”. In: *J Phys Chem B* 109.4 (2005), pp. 1347–1360. URL: ISI:000226626500005.

[25] D Andelman, MM Kozlov, and W Helfrich. “Phase transitions between vesicles and micelles driven by competing curvatures”. In: *EPL (Europhysics Letters)* 25.3 (1994), p. 231.

[26] Rainer Storn and Kenneth Price. “Differential evolution–a simple and efficient heuristic for global optimization over continuous spaces”. In: *Journal of global optimization* 11.4 (1997), pp. 341–359.

[27] Udo Von Toussaint. “Bayesian inference in physics”. In: *Reviews of Modern Physics* 83.3 (2011), p. 943.

[28] H Jeffreys. “Theory of probability,(Oxford: Oxford University Press)”. In: (1961).

[29] Nissim Garti, Dima Libster, and Abraham Aserin. “Lipid polymorphism in lyotropic liquid crystals for triggered release of bioactives”. In: *Food & function* 3.7 (2012), pp. 700–713.

[30] Norbert Kučerka et al. “Molecular structures of fluid phosphatidylethanolamine bilayers obtained from simulation-to-experiment comparisons and experimental scattering density profiles”. In: *The Journal of Physical Chemistry B* 119.5 (2015), pp. 1947–1956. ISSN: 1520-6106. DOI: 10.1021/jp511159q. URL: 25436970.

[31] Benjamin Kollmitzer. “Elasticity and interactions of liquid-ordered/liquid-disordered domains”. PhD Thesis. Graz: Graz University of Technology, Austria, 2015.

[32] Mark W Tate and Sol M Gruner. “Temperature dependence of the structural dimensions of the inverted hexagonal (HII) phase of phosphatidylethanolamine-containing membranes”. In: *Biochemistry* 28.10 (1989), pp. 4245–4253.

[33] N. Kucerka et al. “Lipid bilayer structure determined by the simultaneous analysis of neutron and X-ray scattering data”. In: *Biophys J* 95.5 (2008), pp. 2356–2367. ISSN: 0006-3495.

[34] Stephen H. Alley et al. “X-ray diffraction measurement of the monolayer spontaneous curvature of dioleoylphosphatidylglycerol”. In: *Chemistry and Physics of Lipids* 154.1 (2008), pp. 64–67. DOI: 10.1016/j.chemphyslip.2008.03.007. URL: 18405663.

[35] D. C. Turner and S. M. Gruner. “X-ray diffraction reconstruction of the inverted hexagonal (HII) phase in lipid-water systems”. In: *Biochemistry* 31.5 (1992), pp. 1340–1355.

[36] Joachim Seelig. “31P nuclear magnetic resonance and the head group structure of phospholipids in membranes”. In: *Biochimica et Biophysica Acta (BBA)-Reviews on Biomembranes* 515.2 (1978), pp. 105–140.

Appendix

Guest lipid parameter sets

Table i: Most likely parameter sets for Egg-Sphingomyelin determined by MCMC.
* determined from peak positions. ** calculated by (2.17)

T [°C]	40		50	
x_{SM} [mol%]	10	20	10	20
a * [Å]	84.6	96.7	81.2	92.1
Δ [Å^2]	14.8	23.2	15.6	17.5
n	9	7	12	9
σ_{fluc} [Å]	0.134	0.130	0.14	0.14
b_{SM}/b_{DOPE} **	1.79	1.61	1.64	1.33
C_0 [Å^{-1}]	0.0029	0.0046	0.0017	0.0057
d_H [Å]	10.0	10.0	10.6	9.9
x_{lam}	4.9	6.3	4.7	6.6
$A_{L,lam}$	67.2	64.7	68.1	67.7
$n_{H_2O,lam}$	14.4	16.0	12.3	15.6
λ_1	3.30	3.10	2.56	2.06
λ_0	0.085	0.151	0.046	0.116

Table ii: Most likely parameter sets for DMPC determined by MCMC.
* determined from peak positions. ** calculated by (2.17)

T [°C]	20	30		40		50	
x_{DMPC} [mol%]	10	10	20	10	20	10	20
a * [Å]	92.0	88.2	97.5	84.4	92.9	80.5	89.5
Δ [Å^2]	15.8	14.5	18.1	21.0	29.4	19.0	18.5
n	6	6	4	8	20	9	6
σ_{fluc} [Å]	0.113	0.115	0.110	0.121	0.131	0.123	0.101
b_{DMPC}/b_{DOPE} **	1.90	1.60	1.76	1.61	1.78	1.18	1.11
C_0 [Å^{-1}]	0.0031	0.0008	-0.0007	0.0036	-0.0006	0.0023	0.0033
d_H [Å]	9.9	7.9	9.9	8.6	9.8	2.1	4.0
x_{lam}	5.0	5.3	7.6	4.0	5.4	5.1	8.5
$A_{L,lam}$	64.0	66.8	69.0	60.9	69.2	65.3	68.4
$n_{H_2O,lam}$	12.5	14.4	19.4	6.1	15.9	7.6	15.8
λ_1	1.28	1.18	0.55	1.38	0.87	1.13	0.61
λ_0	0.050	0.055	0.050	0.046	0.049	0.046	0.040

Table iii: Most likely parameter sets for DLPE determined by MCMC.
* determined from peak positions. ** calculated by (2.17)

T [°C]	35		40	50	
x_{DMPC} [mol%]	10	20	10	10	20
a * [Å]	82.9	82.6	80.8	78.3	78.2
Δ [Å^2]	14.0	11.3	12.2	12.1	9.8
n	9	25	14	12	25
σ_{fluc} [Å]	0.160	0.127	0.132	0.145	0.132
b_{DLPE}/b_{DOPE} **	1.82	1.50	1.37	1.21	1.31
C_0 [Å^{-1}]	-0.0100	-0.0201	-0.0082	-0.0075	-0.0199
d_H [Å]	3.0	8.2	8.2	8.1	8.2
x_{lam}	2.0	3.5	3.8	4.3	3.4
$A_{L,lam}$	68.3	60.5	62.3	65.8	59.4
$n_{H_2O,lam}$	10.3	7.2	8.0	10.8	4.4
λ_1	5.0	2.8	3.1	2.7	2.3
λ_0	0.117	0.106	0.124	0.124	0.121

Filler molecule electron densities

As squalene was newly introduced as filler molecule, we determined its electron density by measuring its volumetric mass density. This was done by the *Anton Paar Density Meter DMA 5000M*-apparatus:

$$\rho_{squalene} = 0.86873 + -0.000675 * T \pm 0.0001 \mathrm{g/cm}$$

For tricosene, the volume was estimated by reassembling the molecular groups of POPE and SOPE in [30] and from there, the electron density was calculated. Both electron density curves are plotted in figure i.

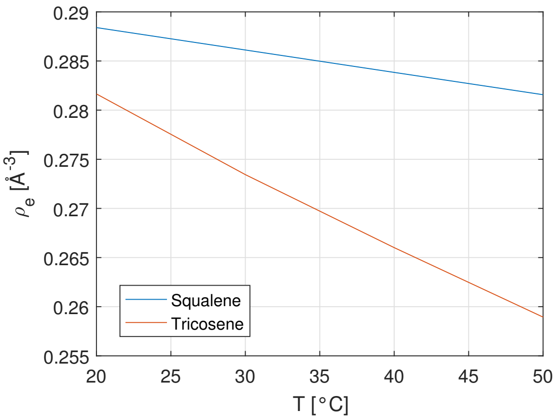

Figure i: Electron densities of squalene and tricosene.